



**Design and Fabrication of Bioelectrodes for Microbial
Bioelectrochemical Systems**

Journal:	<i>Energy & Environmental Science</i>
Manuscript ID:	EE-REV-06-2015-001862.R2
Article Type:	Review Article
Date Submitted by the Author:	21-Aug-2015
Complete List of Authors:	Xie, Xing; California Institute of Technology, Environmental Science & Engineering Criddle, Craig; Stanford University, Civil and Environmental Engineering Cui, Yi; Stanford University, Department of Materials Science and Engineering

Design and Fabrication of Bioelectrodes for Microbial Bioelectrochemical Systems

Xing Xie¹, Craig Criddle^{1,*}, Yi Cui^{2,3,*}

¹*Department of Civil and Environmental Engineering, Stanford University, Stanford, California 94305, USA.*

²*Department of Materials Science and Engineering, Stanford University, Stanford, California 94305, USA.*

³*Stanford Institute for Materials and Energy Sciences, SLAC National Accelerator Laboratory, Menlo Park, California 94025, USA.*

**Correspondence and requests for materials should be addressed to C.S.C (ccriddle@stanford.edu) or Y.C. (yicui@stanford.edu).*

Abstract: Microbial bioelectrochemical systems (BESs) interconvert electrical and chemical energy, enabling electricity generation, hydrogen production, chemical synthesis, wastewater treatment, desalination, and remediation. The focus of this review is design of bioelectrodes for BESs. Desirable features are high conductivity, stability, and biocompatibility. We trace the history of bioelectrode design from nonporous designs to modern porous designs that are particle-based, fiber-based, or monolithic, and compare performance characteristics. The most promising strategies use porous structures conducive to microbial colonization and surface materials that promote efficient electron transfer.

1. Introduction to microbial bioelectrochemical systems

1.1 Background and applications

Microbial bioelectrochemical systems (BESs) harness the metabolic machinery of microorganisms to interconvert electrical and chemical energy¹⁻⁷. Transduction of energy is achieved by microbial colonization of a bio-anode or a bio-cathode and electron transfer to or from bioelectrode surfaces. The microorganisms that mediate these electron transfers are variously referred to as exoelectrogens, electrochemically active bacteria, anode- or cathode-respiring bacteria, or electricigens. For the purposes of this review, we adopt the term “exoelectrogens”. Known exoelectrogens include species in the genera *Shewanella*⁸, *Geobacter*⁹, *Escherichia*¹⁰, *Rhodopseudomonas*¹¹, and *Ochrobactrum*¹² (Figure 1). Exoelectrogens mediate electron transfers between solids and dissolved substances in many natural environments (soils, mines, hot springs, thermal vents, aquifers, lake, ocean sediment) and over a wide range of physical-chemical conditions (pH, ionic strength, pressure, temperature).

Development of BES applications that harness exoelectrogens has grown tremendously since the first report of microbially generated current in 1911¹³⁻³¹. Common BES applications involve electricity generation, hydrogen production, chemical synthesis, wastewater treatment, desalination, remediation, and sensing³²⁻⁴⁸. Microbial fuel cells (MFCs) are the most common BES applications. In these devices, dissolved organic matter is oxidized at a bio-anode, and an oxidant –typically O₂– is reduced at a cathode³²⁻³⁴. In general, a membrane separates the bio-anode from the cathode. A common limitation to MFCs is low efficiency of energy recovery due to voltage and

energy losses⁴⁹. With bio-anode applications, much of these energy losses can be traced to use of O₂ as oxidant but recent innovations make such losses avoidable²⁴. MFCs can be used for desalination, driving cation migration to an anode and anions migration to a cathode^{35, 36}. By adding a reverse-electrodialysis membrane between the anode and cathode, energy can be extracted from salinity gradients in microbial reverse-electrodialysis cells^{37, 38}. Cathodic reactions in BES enable reduction of oxidized contaminants, such as nitrate, perchlorate, sulfate, and organic halides³⁹⁻⁴², production of hydrogen in microbial electrolysis cells^{43, 44}, and reduction of carbon dioxide to produce biofuels^{45, 46}. Both bio-anodes and bio-cathodes can be used in biosensor applications that take advantage of the linear relationship between current and analyte concentration^{47, 48}.

1.2 Life on redox-active surfaces

Exoelectrogens growing on bio-anodes remove electrons from soluble electron donors, such as dissolved organic matter. These electrons are transferred to the surface of the bio-anode, which may be a coating^{23, 50, 51}. For each electron equivalent removed from the electron donor and transferred to the bio-anode, a fraction f_e is oxidized to meet cell energy requirements, and a fraction f_s is used for cell synthesis and maintenance, where $f_e + f_s = 1$ ⁵². The fraction used for energy depends upon the energy generated by transfer of one electron equivalent to the bio-anode surface. The exoelectrogen must obtain enough energy for competition with non-exoelectrogens competing for the same electron donors but using soluble electron acceptors, such as CO₂ or sulfate. In effect, the bio-anode surface “competes” with locally available soluble electron acceptors. After transfer of electrons to the bio-anode, the electrons can flow through an external circuit to

the cathode, but again, only if thermodynamics permits: the cathode potential must be greater than the potential of the bio-anode. It must also be less than the potential of soluble electron acceptors at the cathode. The result is a thermodynamic hierarchy for electron donors and electron acceptors (Tables 1 and 2) that affects the choice of electrode materials and constrains the energy that can be harvested for human use. Similar discuss can be also applied to the bio-cathodes.

1.3 The importance of scale

Considerations of scale are critical for bioelectrode design. Exoelectrogens range in size from a few hundred nm to a few μm , and can grow as biofilms on a diverse range of materials with a range of topography, including two-dimensional surfaces, such as carbon paper, and three-dimensional (3D) media, such as graphene-coated sponge (Figure 1) ^{8-12, 23, 51, 53, 54}. Different processes carry electrons to and from exoelectrogens, including: (1) synthesis of and diffusion of redox-active shuttles; (2) synthesis of redox-active membrane-bound proteins that engage in short-range direct electron transfer with the bioelectrode surface; and (3) synthesis of microbially-generated nanowires (or a solid matrix) that tether the cell to a bioelectrode surface and enable long-range electron conduction ^{1, 21, 26, 55}.

Key scale-dependent factors are the rates of electron transfer, diffusion of substrate and products, and advection. Bioelectrode design influences each process and can determine which is rate-limiting. Delivery of electrons is needed for sustained reduction of an oxidized bio-anode by its attached cells. Removal of electrons is required for sustained oxidation of a reduced bio-cathode by its attached cells. If these electron

transfer rates are slow, the intrinsic rates of substrate utilization can become limited. Such limitations can be addressed with conductive coatings, stainless steel current collectors, and creation of electrode topography that fosters adhesion^{23, 50, 51}. When electron transfer is rapid, diffusion of soluble substrates and products, including delivery of reactants and removal of waste products, can become rate-limiting. Diffusion is fast over the length scale of a bacterium (Table 3), occurring in ms, but because the time required is proportional to the distance squared, diffusion over 1 mm is already dramatically slower (min). Over a scale of centimeters, advection is needed to bring substrates to exoelectrogens, to remove waste products, and to enable acceptable rates of substrate utilization. Diffusion is too slow (days to months).

2. Optimizing electron and solute transfer

The goal of bioelectrode development is to obtain bioelectrodes with high volumetric current density (A/m^3). This parameter is a product of the specific surface area of the electrode (m^2/m^3) and the areal current density (A/m^2) (Scheme 1). The electrode surface must be accessible for microbial colonization. Based upon these considerations, the ideal high performance bioelectrode would combine macroscale and microscale features (Scheme 1). Desirable macroscale features would include a 3D macroscale porous structure that facilitates advective delivery of substrates, improves removal of waste products, and prevents clogging. Desirable microscale features would include conductive coatings and networks and topographic features favorable for efficient microbial adhesion and electron transfer.

The first step in fabricating such a bioelectrode is creation of a conductive and porous 3D scaffold. This can be done by thermal transformation of an insulating template that possesses the desired macrostructure into a conductor^{31, 56-67}, or by coating a template with stable, biocompatible, and conductive materials, such as inert metals, carbon nanotubes (CNTs), graphene, or conductive polymers^{8, 23, 50, 68}. A 3D porous scaffold can also be fabricated directly from conductive elements, say, for example, by incorporating conductive nanomaterials, graphite granules, graphite fibers, and inert metal wires⁶⁹⁻⁷⁷. Key parameters of the 3D porous electrode include pore size, pore shape, macro-porosity, and accessibility (open or closed) (Scheme 1). Surface modifications can increase microbial adhesion and electron transfer. The common strategy is to increase the electrode conductivity, micro-porosity, roughness, hydrophilicity, biocompatibility, or charge storage capacity (Scheme 1). Many research groups have developed such electrodes, using chemical and thermal treatments and a variety of coatings, including redox-active additives, conductive polymers, and nanomaterials⁷⁸⁻⁹⁰. Good reviews of these surface modification studies are available⁹¹⁻⁹³.

In the following sections, we focus on the structural design of a porous and conductive 3D scaffold. We summarize design of traditional nonporous BES bioelectrodes (Scheme 2A), then discuss porous bioelectrodes, including configurations that are particle-based (Scheme 2B-D), fiber-based (Scheme 2E-I), and monolithic (Scheme 2J-L). For each category, we provide examples of bioelectrodes that have been investigated in BESs (Table 4). We discuss whether the reported bioelectrodes are truly open and capable of internal colonization. Given the size of exoelectrogens (a few hundred nm to a few μm) (Figure 1)^{8-12, 23, 51, 53, 54}, microscale pores less than a few μm

are not accessible for colonization. We also examine the time period for operation and potential for long-term clogging. We define “long-term studies” as those with minimal operational periods of at least a few months. Since the thickness of mature biofilms ranges from tens of μm to hundreds of μm ^{9, 94}, only those electrodes with pore size of at least a few hundred μm are expected to be sustainable without clogging. Key performance metrics are the maximum current densities normalized to the projected/total surface area or bioelectrode volume. Because these metrics are difficult to compare for different systems, we include a description of BES operation, the nature of the microorganisms used, substrates supplied, and method of measurement of current densities (fixed anode potentials, polarization curve, or operation with an external load). Despite our inclusion of these factors, direct comparison of bioelectrode performance remains challenging as we lack information on electrode thickness, long-term sustainable current output, and clogging. No studies have measured the real electrode-biofilm interfacial area, a parameter that is more directly related to the structure design of the bioelectrode. In addition, assessment of most bioelectrodes has occurred in synthetic electrolytes prepared with dissolved solutes and purified water, limiting extrapolation of bioelectrode performance to real wastewaters containing suspended particles.

2.1 Nonporous bulk electrodes

2.1.1 Carbon electrodes

Traditional graphite electrodes, such as graphite rods, graphite plates, or graphite disks, are commonly used due to their low cost, high conductivity, high stability, and biocompatibility (lack of microbial toxicity and resistance to microbial degradation)^{33, 34}.

⁹⁵. The graphite surface appears rough at the 10 μm scale (Figure 2A), but nearly flat at the one μm scale of exoelectrogens (Figure 2B). To improve microbial attachment and electron transfer, experts have modified these electrodes using multi-walled carbon nanotubes (MWCNTs) ⁹⁶, a MWCNT/SnO₂ nanocomposite ⁹⁷, a MWCNT/MnO₂ nanocomposite ⁹⁸, in-situ exfoliated graphene ⁹⁹, Au/Pd nanoparticles ¹⁰⁰, a graphite paste containing Fe₃O₄ or Fe₃O₄ and Ni²⁺ ¹⁰¹, polyaniline nanostructure ¹⁰², a sulfonated polyaniline/vanadate composite ¹⁰³, positively charged groups reduced from aryl diazonium salts ⁵³, a capacitive layer consisted of a mixture of activated carbon powder and a N-methyl-2-pyrrolidone/poly(vinylidene fluoride) solution ¹⁰⁴, and redox-active aromatic compounds, such anthraquinone-1,6-disulfonic acid and 1,4-naphthoquinone ¹⁰¹. Even with those surface modifications, the maximum current densities achieved are normally not higher than 10 A/m² (Table 4) ^{95-99, 103, 104}.

2.1.2 Metal electrodes

Researchers have prepared bioelectrodes using gold, platinum, and titanium. Richter et al. demonstrated biofilm growth of *G. sulfurreducens* on gold (Figure 2 C and D) with current density of 0.4-0.7 A/m². The electrodes were polarized at 0.3 V vs Ag/AgCl in an acetate medium. Confocal laser scanning microscopy indicated a biofilm thickness of about 40 μm ⁹. Crittenden et al. investigated surface modification of gold electrodes with self-assembled monolayers of carboxylic acid terminated alkanethiols. The modification enhanced the electronic coupling of *S. putrefaciens* to gold electrodes. When lactate was used as the electron donor, a modified gold electrode could achieve a peak current output of $\sim 3.8 \times 10^{-3}$ A/m², a value that is about 3 times greater than that of a glassy carbon electrode operating under the same conditions ($\sim 1.2 \times 10^{-3}$ A/m²) ¹⁰⁵. Liu et

al. prepared gold electrodes by electroplating gold onto a silicon wafer. Two kinds of electrodes were designed with the same exposing gold surface areas but different patterns: one was rectangular and the other was an array of 10 μm wide lines spaced 100 μm apart (Figure 2 E and F). When the electrodes were polarized at 0.24 V vs. SHE in an acetate medium seeded *G. sulfurreducens*, the line array electrode achieved a 4-fold higher current output (16 vs. 4 A/m^2). Confocal laser scanning microscopy and SEM images (Figure 2 G and H) revealed that the current output was elevated mainly by the increased biomass: cells could grow at least 15 μm outward in a semicylinder from the gold lines, resulting in 4-fold more biomass on the line array electrode¹⁰⁶. In another study, different electrodes were evaluated in MFCs seeded with anolyte from a previous MFC and fed acetate: a platinum-coated titanium electrode enabled higher maximum current densities ($\sim 4.1 \text{ A}/\text{m}^2$) than a flat graphite electrode ($\sim 3.0 \text{ A}/\text{m}^2$), but the same graphite electrode blasted with aluminum oxide enabled even higher current densities ($\sim 4.6 \text{ A}/\text{m}^2$)¹⁰⁷. Maximum current densities were estimated from polarization curves. While the capital cost of precious metal bioelectrodes is high, they could have value for small-scale BES applications.

Stainless steel is a less costly alternative to precious metals. To date, the main application of stainless steel electrodes is in marine MFCs^{108, 109}. These electrodes were pretreated with acid (2% HF/0.5 M HNO_3 for 20 min) to remove the oxide layer^{72, 108}. Erable and Bergel reported a maximum current density of 4 A/m^2 when a stainless steel plate electrode was polarized at -0.1 V vs SCE in an acetate medium inoculated with a natural biofilm scraped from harbor equipment⁷².

Baudler et al. systematically studied several metal anodes, including copper, gold, silver, stainless steel, nickel, cobalt, and titanium, in parallel with a graphite anode⁹⁴. For bioelectrochemical measurements, these electrodes were polarized at 0.2 V vs. Ag/AgCl (for graphite, gold, and silver) or -0.2 V vs. Ag/AgCl (for copper, steel, nickel and titanium) in an acetate solution seeded with preselected bacterial cultures from wastewater. The copper anode achieved the highest current output (15.15 A/m²), followed by gold (11.75 A/m²), silver (11.19 A/m²), graphite (9.84 A/m²), stainless steel (6.74 A/m²), and nickel (3.84 A/m²). These current densities correlated with the thickness of the electrochemically active biofilms that developed on the anodes, which were 249±21 μm, 127±11 μm, 154±10 μm, 117±13 μm, and 77±9 μm, for copper, gold, silver, graphite, and nickel, respectively (Figure 2I). In general, thicker biofilms developed at higher current density. The authors also estimated material costs for production of electrodes with comparable electric conductivities. Because of the superior conductivity of copper, the thickness of copper electrode could be much thinner and thus material cost (0.53 US \$/m²) is significantly lower than those of graphite (26.1 US \$/m²) and stainless steel (9.47 US \$/m²) electrodes.

For nonporous bulk electrodes, exoelectrogens only grow on the outer surface (Scheme 2A), so the interfacial area is limited to the projected geometric surface area of the electrode. This prevents further increases in current density, given that only those exoelectrogens growing within a certain distance of the electrode surface can effectively contribute to current generation.

2.2 Particle based porous electrodes

2.2.1 Densely piled electrodes

Particle “piling” is commonly used to prepare 3D porous electrodes for traditional electrochemical systems, such as batteries and fuel cells. This method is also widely used for bioelectrode fabrications. Zhang et al. used a roller press to prepare bioelectrodes from an emulsion of graphite particles (5 μm diameter) mixed with polytetrafluoroethylene (PTFE) ¹¹⁰ at different percentages (6-48%) ¹¹¹. The authors found that 30% PTFE is optimal: in addition to serving as a binder, PTFE increased the porosity and wettability of the composite electrode, facilitating microbial attachment and electron transfer. At high PTFE content, however, electric conductivity decreased, and thick bio-films formed that clogged the pores. The electrodes were tested in a single chamber MFC where the anode chamber was flushed with electrochemically active *E. coli* and a glucose medium. For a constant load of 1.98 k Ω , the electrode with 30% PTFE initially achieved a maximum current output of $\sim 1.2 \text{ A/m}^2$, but gradually dropped to $< 0.5 \text{ A/m}^2$ after 10 h.

In some studies, the particles filled the pore space of current collectors made from stainless steel meshes, carbon felts, or nickel foam, but open porous structures were not achieved. In a typical fabrication, Zhang et al. used a paste prepared by mixing of graphene powder with PTFE to coat the surface of a stainless steel mesh. The composite electrode was then pressed ¹¹². Peng et al. prepared a paste by mixing activated carbon/goethite powders with PTFE. The paste was roll-pressed into a sheet 0.2 mm in thickness then roll-pressed onto a stainless steel mesh current collector ¹¹³. Wang et al. have created polyaniline/mesoporous tungsten trioxide (WO_3) composites or nanomolybdenum carbide (Mo_2C)/CNT composite with PTFE suspensions coated onto carbon

felt^{10, 114}. A pressing procedure was used to improve electrical contact, but this protocol likely changed macroscale porosity. Figure 3A and B show the polyaniline/WO₃ composite electrode before and after colonization. The pore size is less than 100 nm, and is thus not accessible to exoelectrogens. Qiao et al. coated nickel foams with a paste prepared by mixing MWCNT/polyaniline or TiO₂/polyaniline composite powders with PTFE. They then applied a pressing procedure to improve electrical contact (Figure 3C-E)^{115, 116}. The same procedure was applied by Zhao et al. to coat nickel foams with nanostructured graphene/TiO₂ hybrids¹¹⁷. The maximum current densities achieved with these pressed composite electrodes were in the range of 0.15-19 A/m², all of which were estimated from polarization curves. Additional detailed are provided in Table 4^{10, 112-117}.

Although high current densities are achieved, applying pressure to pile up nm to μm scale particles results in nm to μm scale pores (Figure 3) that exoelectrogens could clog but not effectively colonize. The thickness of these biofilms ranged from tens of μm to hundreds of μm . Because the exoelectrogens could only grow on the outer surface of the electrode, performance was like that of nonporous electrodes with improved electrode surfaces (Scheme 2B).

2.2.2 Cell-embedded electrodes

Several research groups have blended microorganisms and electrode materials in an effort to increase interactions between microorganisms and the electrode (Scheme 2C). In a typical fabrication, anodic microorganisms from a MFC were harvested, mixed with carbon nanoparticles (300 nm) and PTFE, and the resulting paste was spread on a carbon cloth current collector (Figure 4A)¹¹⁸. Cho et al. mixed permeabilized *Ochrobactrum*

anthropi SY509 cells directly with copper powders (<65 μm in diameter). An acrylic mold filled by the mixture was soaked in a CaCl_2 solution for hardening, and a microorganism/copper composite bioelectrode was ready after 3 h (Figure 4B)¹¹⁹. Liang et al. added MWCNT powders into the anolyte simultaneously with an inoculum of *G. sulfurreducens*, incorporating MWCNTs into the anodic biofilm matrix and forming a composite biofilm on a carbon paper current collector (Figure 4C)¹²⁰. Another group added graphene oxide to anolyte containing microorganisms, creating a bacteria/graphene network¹²¹. Park et al. immobilized *E. coli* on $\text{Fe}_3\text{O}_4/\text{CNT}$ nanocomposite by a culturing process for 2-3 h then loaded the resulting network onto a carbon paper electrode¹²². Although these research teams achieved a large exoelectrogen-electrode interfacial area, the thickness of the composite bioelectrodes was limited to a few hundreds of μm . Under such conditions, the macroscale pores needed for substrate transport into/out of the biofilms are absent, and exoelectrogens within the matrix become inactive. Electrodes prepared with pre-embedded exoelectrogens cannot sustain microbial activity. The maximum current densities reported in these studies were less than 9 A/m^2 , estimated from polarization curves (Table 4)^{118, 121, 122}.

2.2.3 Packed bed electrodes

To achieve open 3D structures with macroscale pores that are accessible to exoelectrogens but do not clog (Scheme 2D), researchers have used mm scale granules, such as granular graphite (Figure 5A) and granular activated carbon (Figure 5B)^{69, 70, 123}. Rabaey et al. fabricated a tubular MFC with a 390 mL anode compartment filled with graphite granules between 1.5 and 5 mm in diameter (Figure 5C). The packed bed of graphite granules had a porosity of 0.53 and specific surface area of $817\text{-}2720 \text{ m}^2/\text{m}^3$. To

improve substrate transport, anolyte was circulated through the porous anode at a rate of 100 mL/min. After seeding with a bacterial culture obtained from previous MFC, the tubular acetate-fed MFC achieved a maximum current generation of 31 mA through a 20 Ω external resistor after 26 days of operation. The maximum current density based on the volume of the anode (390 mL) was $\sim 80 \text{ A/m}^3$ ⁶⁹.

Aelterman et al. investigated acetate-fed MFCs containing packed bed anodes fabricated from 2 mm or 5 mm diameter graphite granules. The anode compartment (156 mL) was seeded with anolyte from a previous MFC. External resistance was gradually decreased from 50 Ω to 10.5 Ω over a 150 day period of operation. The MFCs containing 2 mm or 5 mm graphite granules achieved current densities of $\sim 150 \text{ A/m}^3$ and $\sim 250 \text{ A/m}^3$, respectively. The authors argued the 2 mm graphite granules had more contact points and higher internal resistance, resulting in lower power density ⁷⁰. Researchers have also used granular activated carbon granules for packed bed bioelectrodes ^{124, 125}. The electrode surface area is increased, but the pores of the activated carbon are sub- μm and thus inaccessible to exoelectrogens. A drawback to use of activated carbon compared to graphite is that it normally has a lower conductivity, and thus greater potential for increased internal resistance.

In another study, Wang et al. coated crumb rubber granules (4-8 mm) from recycled tires with a conductive graphite paste and allowed the paste to dry. A 140-mL anode MFC chamber was filled with the coated granules, seeded with anaerobic digester sludge, and fed acetate. From the polarization curve, the maximum current density achieved was $\sim 1 \text{ A/m}^3$, less than that of graphite granules (2-6 mm) under the same conditions ($\sim 1.5 \text{ A/m}^3$). The coated rubber granules had a higher specific surface area, but conductivity

was lower. The loose packing of the coated rubber granules (1.1 g/cm^3 vs. 2.2 g/cm^3 for graphite granules) may have increased internal resistance, but decreased the energy needed for analyte flow ⁷¹.

2.3 Fiber based porous electrodes

2.3.1 Carbon paper/cloth/mesh electrodes

Carbon paper (Figure 6A-C) and carbon cloth (Figure 6D-H) are the most commonly used and commercialized bioelectrode materials in BESs. To fabricate carbon paper, evenly piled graphite fibers, a few μm in diameter (Figure 6B), are compressed into a thin and brittle sheet (Figure 6A). To fabricate carbon cloth, hundreds of individual graphite fibers are bundled, then regularly woven into a piece of flexible cloth (Figure 6D). Both carbon paper and carbon cloth are highly conductive, with sheet resistances less than $1 \Omega/\text{sq}$.

Several research groups have improved the current density of carbon paper and carbon cloth. Researchers suspended Pt loaded MWCNTs, polypyrrole-coated MWCNTs, or graphene/Au composites in a solution then spread the solution over carbon paper ¹²⁶⁻¹²⁸. He et al. modified carbon paper by plasma-based N^+ ion implantation. The treated carbon paper had higher surface roughness and hydrophilicity ¹²⁹. Zhang et al. decorated carbon paper with mesoporous carbons using a layer-by-layer self-assembly method ¹³⁰. Guo et al. constructed multilayer polyethyleneimine/graphene films on carbon paper ¹³¹. Liu et al. applied an electrochemical method to deposit a CNT network on carbon paper ¹³². They also simultaneously deposited CNTs and chitosan by the same method (Figure 6C) ^{133, 134}. Materials scientists have also modified carbon clothes with conductive polymers (e.g.

polyaniline (Figure 6E)^{135, 136} and polypyrrole¹³⁷), nanomaterials (e. g. MWCNTs (Figure 6F)¹³⁸, bamboo-like nitrogen-doped CNTs¹³⁹, graphene reduced from graphene oxide^{135, 140}, crumpled graphene particles (Figure 6G)¹⁴¹, reduced graphene oxide/SnO₂ nanocomposite¹⁴²), and N-rich molecules (e. g. 4(N,N-dimethylamino)benzene diazonium tetrafluoroborate¹⁴³). These additives were applied as coatings via electrochemical deposition or by chemical reactions, or made into inks or slurries then painted to the carbon cloth. Researchers have also activated the surface of carbon cloth by electrochemical oxidation in different solutions, such as ammonium bicarbonate, ammonium nitrate, ammonium sulfate, nitric acid, and phosphate buffer¹⁴⁴⁻¹⁴⁶.

The spacing between the graphite fibers in carbon paper and carbon cloth is about ten μm (Figure 6A, B and D). In long-term operation, these small pores are easily clogged. Moreover, some of the electrode modifications mentioned above significantly reduce spacing (Figure 6E), bridge the gaps between fibers (Figure 6F), or even completely fill the gaps (Figure 6C and G) in carbon paper and carbon cloth^{136, 138, 141}. Long-term studies of biofilm growth upon these surfaces have shown that biofilm covers only the projected geometric surface of the electrodes with no colonization of inner fibers (Scheme 2E and F, Figure 6H and I)^{8, 23, 147}.

Research teams have also investigated carbon mesh as a BES bioelectrode. Carbon mesh is similar to carbon cloth, but has a more open structure due to a coarser weave. The capital cost of the mesh is much less than that of carbon cloth and the electrode surface can also be modified to achieve better performance¹⁴⁸⁻¹⁵⁰. To date, however, there is no evidence that a carbon mesh can maintain the open porous structure needed for microbial colonization and long-term operation. The maximum current densities

achieved by carbon paper, carbon cloth, or carbon mesh bioelectrodes are usually less than 10 A/m^2 (Table 4)^{126, 127, 129-132, 135-140, 142, 145, 146, 148}, an upper limit similar to that of nonporous carbon electrodes.

2.3.2 Stainless steel mesh electrodes

Stainless steel mesh also has a woven structure similar to that of carbon cloth, but at a larger scale. Because of its excellent mechanical properties, the diameter of stainless steel wire and the spacing between wires can vary from tens of μm to tens of mm . A stainless steel grid electrode generated a maximum current density of 8.2 A/m^2 when polarized at -0.1 V vs SCE in an acetate-fed medium inoculated with a natural biofilm scraped from harbor equipment⁷². Lamp et al. described the effects of carbon nanostructures deposited onto stainless steel meshes (wire diameter, $400 \mu\text{m}$; spacing, about $860 \mu\text{m}$) by a flame synthesis method (Figure 7A-F)¹⁵¹. The modification significantly improved the affinity of the electrode surface for microbial colonization (Figure 7C and F). Erbay et al. directly grew MWCNTs on stainless steel meshes using a water-assisted chemical vapor deposition method⁹⁰. Different physical properties (e.g. length, packing densities, surface conditions) of CNTs were investigated. An electrode modified by long and loosely packed CNTs without any amorphous carbon showed best performance. Based on a polarization measurement in a two chamber MFC inoculated with wastewater and fed acetate, this electrode achieved a maximum current density of $\sim 6 \text{ A/m}^2$. One layer of stainless steel mesh functions as a planar porous bioelectrode, and a 3D electrode configuration is achieved by stacking several layers of stainless steel mesh (Scheme 2G).

2.3.3 Carbon felt electrodes

Carbon felt is a nonwoven material made from carbon fibers that has more open porous structure and can be much thicker than carbon cloth. Carbon fibers are randomly intertwined to form a loose but conducting matrix (Figure 8A and B), and the spacing between the fibers can range from tens of μm to hundreds of μm . Scott et al. coated various carbon/polymer materials onto carbon felt¹⁵². Chen et al. modified carbon felt by pasting it with a solution of porous carbon and PTFE¹⁵³. It was not clear, however, whether the electrodes achieved macroscale porosity: the coating methods were not clearly described and scanning electron microscope (SEM) images of the modified carbon felt electrode surface show only microscale features.

Materials scientists have identified some surface modifications that clearly do preserve the open porous structure of carbon felt. Cercado-Quezada et al. modified the fiber surface of carbon felt by anodisation: the carbon felt electrode was polarized at a high potential, oxidizing some of the carbon on the fiber surface and creating micro-cavities less than 1 μm in diameter (Figure 8E)⁸⁸. Some researchers directly grew CNTs or carbon nanofibers on a fiber surface by chemical vapor deposition (Figure 8C and D)^{78, 79}. Adachi et al. coated carbon felt with a mediator –a derivative of 9,10-anthraquinone-2,6-disulfate– using a solution-based dip-and-dry process⁸⁷. Li et al. modified carbon felt electrodes with two conductive polymers, polyaniline and poly(aniline-co-o-aminophenol), through direct solution based polymerization under acidic conditions⁸⁶. Tang et al. coated a mixture of conductive polypyrrole hydrogels and CNTs composite onto carbon felt⁸³. Cui et al. prepared carbon felt electrodes by electropolymerization of polyaniline on the surface followed by electrophoretic

deposition of CNTs⁸². In other studies, capacitive materials (e.g. MnO₂, RuO₂, polypyrrole/graphene oxide composite, polypyrrole/9,10-anthraquinone-2-sulfonic acid sodium salt composite) were electrochemically deposited on a carbon felt electrode (Figure 8F and G)^{81, 84, 85, 154}. Zhao et al. have also electrochemically deposited polyaniline nanowire networks onto a carbon felt (Figure 8H and I)⁸⁰. The maximum current densities of the resulting carbon felt electrodes were up to 35.7 A/m² and 6 kA/m³, as summarized in Table 4. In some cases, the thickness of the carbon felt was not reported, precluding an estimate of the volumetric current density. The open structure and large pores of the electrode would enable colonization of both the outer and inner surface of the composite electrode (Scheme 2H), but operational time in most of these studies was only 80 h to about 2 months. It is therefore unclear whether the high current density porous 3D structure is sustainable in long-term operation.

2.3.4 Carbon brush electrodes

Brush electrodes, first developed by Garshol and Hasvold for galvanic seawater cells, consist of two or more wires twisted together to form an electrode stem with conducting fibers clamped between the wires¹⁵⁵. Logan et al. used this design to fabricate brush bioelectrodes by winding graphite fibers (average diameter, 7.2 μm) into a twisted core consisting two titanium wires (Figure 9)²². A small brush with 2.5 cm diameter and 2.5 cm length has a porosity of 95% and surface surface-volume ratio of 18200 m²/m³, while a larger brush with 5 cm diameter and 7 cm length has a porosity of 98% and surface-volume ratio of 7170 m²/m³. The authors reported that the brush electrode provided an open structure with high surface area for microbial colonization (Scheme 2I). The resulting graphite brush could undergo ammonia gas treating, acid soaking, and/or

heating to improve the surface affinity^{22, 74}. Estimated from the polarization curves, the maximum current density could be achieved was about 1 kA/m³. A concern with this electrode is that the spacing between graphite fibers becomes more confined near the center of the brush, likely limiting microbe-electrode interactions at these locations.

2.3.5 Carbon nanotube coated textile electrodes

In many studies, researchers have simply sought to modify commercialized electrodes for BESs, but some have developed bioelectrodes specifically for BESs. Xie et al. developed a CNT-textile composite electrode by conformally coating a CNT layer (200 nm) on a macroscale porous textile made of randomly intertwined polyester fibers with diameters of approximately 20 μm (Figure 10A-D)²³. The resulting CNT-textile electrode had a 3D open structure similar to that of the carbon felt electrodes discussed previously. The spacing between the CNT coated fibers ranged from tens of μm to hundreds of μm . The CNT coating layer functioned as an electron pathway and provided an affinitive surface for microbial attachment and extracellular electron transfer. A CNT-textile composite electrode (1 cm \times 1cm \times 0.2 cm) was tested as the anode of a two-chamber glucose-fed MFC inoculated with domestic wastewater. The cross-sections SEM image of the CNT-textile bioelectrode after 55 days of operation showed microbial biofilms wrapped around both exterior and interior CNT-textile fibers (Scheme 2H, Figure 10E). The resulting exoelectrogen-electrode interfacial area was calculated to be 10-fold larger than the projected geometric surface of the bioelectrode. The conformally coated microscale porous CNT layer displays strong interactions with exoelectrogens, including affinitive mechanical contact and higher electrical conductivity (Figure 10F and G). Biofilms were still visible on the CNT-textile fiber surfaces after 5 min of bath

sonication and 10 s of vortex agitation, indicating strong attachment (Figure 10H). From linear staircase voltammetry, the maximum current density achieved by the CNT-textile bioelectrode was 14.4 A/m^2 or 7.2 kA/m^3 .

2.3.6 Carbonized textile/fiber electrodes

Wang et al. fabricated textile electrodes by carbonizing a commercial towel at $1000 \text{ }^\circ\text{C}$ for 30 min under N_2 gas⁶⁵. The carbonized textile had an open structure with freely standing mm scale threads (Figure 11 A-D). The electrode was polarized at 0.3 V vs. Ag/AgCl in an acetate solution seeded with wastewater bacteria. A maximum current density of 8 A/m^2 resulted. SEM images (Figure 11 E-I) demonstrated internal colonization by microbial biofilms. Because the electrode was only operated for <10 days, long-term performance remains unclear. Other researchers have prepared electrodes with nonwoven configuration by carbonizing a polymer fiber network, generated via electrospinning or solution blowing^{31, 156}. To test their performance as MFC bio-anodes, the electrodes were polarized at 0.2 V vs. Ag/AgCl in an acetate solution seeded with wastewater bacteria. A maximum current density of 30 A/m^2 was generated, but this high current density was sustainable for only a few days. Manickam et al. also applied electrospinning to fabricate an activated carbon nanofiber electrode⁶³. This electrode was tested in a single chamber MFC treating wastewater. The maximum current density obtained was about 2.7 kA/m^3 , based on a polarization measurement. The advantage of electrospun or solution blown fibers is that it is normally a single continuous fiber, forming a more continuous pathway for electron flow. On the other hand, the resulting structure is more compact and the pores smaller compared to carbon felt or the CNT-textile electrodes. The spacing between the fibers was only $\sim 1 \text{ } \mu\text{m}$ (Figure 11J). With

such small pore size, the biofilm can only cover the external surface instead of the surface of every fiber. This was confirmed by the SEM images of the electrode colonized by *P. aeruginosa* and *S. oneidensis* MR-1 (Figure 11K and L).

2.4 Monolithic porous electrodes

2.4.1 Reticulated vitreous carbon electrodes

A monolithic porous electrode means that the electrode is porous but the material is intrinsically interconnected as a single unit. The most commonly used monolithic porous electrode material is reticulated vitreous carbon (RVC), also known as carbon foam. RVC is a 3D open porous glassy carbon material made from polymer sponge through carbonization¹⁵⁷. RVC was classified into different grades based on the number of pores per unit length, normally from 10 to 100 PPI (pores per inch (Figure 12A-D). Depending on the PPI grade, RVC has a free void volume between 90% and 97% and a specific surface of 500-7000 m²/m³ (Figure 12E)¹⁵⁷.

RVC electrodes have been employed in BESs. He et al. used RVC (10 PPI) to fabricate bio anodes in an upflow MFC (total volume of 190 cm³) (Figure 12F and G)¹⁵⁸. The MFC was seeded with anaerobic sludge then continuously fed sucrose. From the polarization curve, the maximum volume-based current density was about 50 A/m³. The reactor operated for 5 months, but clogging was not investigated. At a smaller pore size, a 60 PPI RVC electrode was investigated as the bio-anode of a MFC⁶⁶. This material had a free void volume of 96.5% and specific surface area of 3750±90 m²/m³. The strut width was 100 µm and the average pore size was ~320 µm. Pores with diameters <180 µm clogged after 6 month operation. Ringeisen et al. applied a RVC electrode (0.6 cm³) with

a specific surface area of $6070 \text{ m}^2/\text{m}^3$ (true surface area, 37 cm^2) as the anode in a mini-MFC with a cross-section of 2 cm^2 and a volume of 1.2 cm^3 ⁶⁷. The mini-MFC was seeded with *S. oneidensis* DSP10 and fed lactate. Maximum current density obtained from short circuit current was $0.1 \text{ A}/\text{m}^2$ based on the true surface area and $\sim 600 \text{ A}/\text{m}^3$ based on the electrode volume. This report described only 7 days of operation, so long-term performance cannot be assessed. As with other carbon electrodes, Yuan and Kim modified RVC by electrodeposition of polypyrrole to improve the surface affinity for microbial attachment and current generation (Figure 12H) ¹⁵⁹. Flexer et al. directly grew CNTs on a 45 PPI RVC electrode by chemical vapor deposition. The composite electrode was polarized at 0 V vs. Ag/AgCl in an acetate solution seeded with anolyte from a previous MFC. Over a 20-day period of operation, the electrode achieved a peak current output of $68 \text{ A}/\text{m}^2$ based on the projected geometrical surface area (1 cm^2), $0.4 \text{ A}/\text{m}^2$ based on the true surface area, and $10.3 \text{ kA}/\text{m}^3$ based on the electrode volume ⁸⁹.

2.4.2 Other sponge template electrodes

Conversion of the entire sponge into a conductive matrix via carbonization is not necessary to achieve a porous conductive 3D bioelectrode. Another strategy is to apply a thin conductive layer onto the sponge template. Using on a polyurethane sponge template, Liu et al. used chemical vapor deposition to fabricate a nickel-coated 3D sponge (Figure 13A and B) ¹⁴⁷. Thorne et al. coated the polyurethane sponge with titanium oxide (TiO_2) via a slurry coating method. After drying, the TiO_2 -coated sponge was heated to $600 \text{ }^\circ\text{C}$ (1 h) to remove the polymer template then further heated to $1300 \text{ }^\circ\text{C}$ (4 h) to sinter the ceramic. Electron transport pathways were created by chemical vapor deposition of a thin layer of fluorine doped tin oxide ¹⁶⁰. Xie et al. coated polyurethane sponges with a thin

layer of conductive CNTs or graphene using a solution-based dipping-and-drying method (Figure 13C-E)^{50,51}. The CNT-sponge composite electrode (pore size range of 300~500 μm) was investigated as a bio-anode in a traditional H-shaped MFC inoculated with anolyte from a previous MFC seeded with domestic wastewater. In a glucose medium, the CNT-sponge achieved a current density maximum of 21.3 A/m^2 or 10.6 kA/m^3 . SEM images revealed dense microbial biofilms within the bioelectrode with macroscale pores that were not clogged by the microbial growth after 1 year of operation (Scheme 2J, Figure 13F).

In another study, nickel foam with the same 3D sponge-like structure was used the temple for a graphene/polyaniline hybrid electrode (Figure 13G)⁸. Chemical vapor deposition was used to deposit graphene onto the nickel foam matrix (1 $\text{cm} \times 1\text{cm} \times 0.1$ cm), and the matrix was subsequently dissolved away with hydrochloride acid (HCl). Polyaniline was deposited onto the graphene surface by *in situ* polymerization. The resulting graphene/polyaniline composite electrode inherited the 3D open porous structure from the original nickel foam, with pores of 100-300 μm . The hybrid anode was tested in an *S. oneidensis* MR-1 seeded two-chamber MFC using lactate as electron donor at the anode and potassium hexacyanoferrate ($\text{K}_3\text{Fe}(\text{CN})_6$) as electron acceptor at the cathode. Polarization curves indicated a maximum current density about 5 A/m^2 or 5 kA/m^3 . Internal colonization was confirmed by interior SEM images of the electrode harvested after 60 h of operation in a MFC (Figure 13H). Long-term clogging was not investigated. Wang et al. and Qiao et al. also reported use of graphene/Ni foam composite electrodes, but without dissolution of the Ni foam templates^{161,162}.

2.4.3 Corrugated fiberboard template electrodes

Another material used as a bioelectrode template is corrugated fiberboard⁶⁴. Commercially available corrugated fiberboard consists of a flute layer sandwiched between two liner layers, creating a layered assemblage that is a few mm in thickness. Macroscale channels on the scale of mm were formed between the flute layer and the two liner layers. Carbonization at 1000 °C under nitrogen for 1 h created conductive layered corrugated carbon (LCC) (Figure 14A). To test its performance for current generation, the LCC electrodes were polarized at 0.2 V vs. Ag/AgCl in an acetate solution seeded with preselected bacterial cultures from wastewater (Figure 14B and C). A 2.2 mm thick LCC achieved a maximum current density of $\sim 70 \text{ A/m}^2$ or $\sim 32 \text{ kA/m}^3$ based on volume. The areal current density increased to 390 A/m^2 when 6 of the corrugated carbon layers were stacked together, while the volumetric current density remained similar (Figure 14D). These results are the highest current density achieved by microbial electrodes so far, and can be largely attributed to the macroscale-channeled structure. With mm scale spacing, these macroscale channels were well suited for internal colonization. The same team also studied the long-term performance of the LCC electrodes¹⁶³. Peak current output decreased only slightly after about 100 days of operation. Digital photographs of the electrodes taken after at least 25 batch cycles clearly show that the channels did not become blocked.

2.4.4 Natural template electrodes

Natural templates can also be used to fabricate 3D porous electrodes^{56, 57}. For example, dry kenaf (*Hibiscus cannabinus*) stems were collected and carbonized at 1000 °C under nitrogen (Figure 14E). The resulting electrode (3D-KSC) maintained the structure of the kenaf stem: a hollow tube with an outer diameter of 10 mm, an inner

diameter of 4 mm, and a highly ordered macroporous wall revealing two types of channels with diameters of 25 μm and 60 μm , respectively (Figure 14F-K). These 3D-KSC anodes were polarized at 0.2 V vs Ag/AgCl in MFCs seeded with domestic wastewater and fed acetate. In batch mode, a maximum current density of 32.5 A/m^2 was achieved with a small 3D-KSC anode (length, 0.23 cm; external surface: 1.52 cm^2). SEM images indicated that the biofilms grew on both the external surface and inside the channels, but penetrated less than 100 μm even when the media was flow through the center chamber (Figure 14L-O). A likely reason is blockage of the channels by valves with small holes (Figure 14I-K) (a few μm). For such a structure, internal colonization of the entire 3D electrode would require removal of the valves an opening of the channels. Another natural template that has been evaluated by the same team is sponge-like pomelo peel⁵⁷. Reticulated carbon foam was obtained after carbonization. The maximum current density achieved was $>40 \text{ A}/\text{m}^2$, or 18 kA/m^3 (Table 4). Karthikeyan et al. picked three plants for carbonization, including corn stem, king mushroom, and wild mushroom⁵⁸. The maximum current densities based on the projected geometric surface area were 31.2 A/m^2 , 20.9 A/m^2 , and 30.2 A/m^2 , respectively, while the corresponding volumetric current densities were or 15.6 kA/m^3 , 10.5 kA/m^3 , and 15.1 kA/m^3 , respectively (Table 4). Other natural templates evaluated to date include tubular bamboo and loofah sponge^{59, 60, 164}. Applying natural templates may reduce the cost of the bioelectrodes, but could have intrinsic structural limitations that are difficult to overcome.

2.4.5 Self-made template electrodes

Instead of using commercially available materials, some research groups have applied self-made templates. Nguyen et al. used a wet phase inversion process to prepare

a mesoporous polysulfone support matrix. The pore size of the matrix was $\sim 100 \mu\text{m}$ and the porosity was $\sim 90\%$. They then coated the matrix with a thin layer of conductive CNTs using a solution-based dipping-and-drying method. The composite electrode was investigated in a two-chamber cube shape MFC inoculated with *S. oneidensis* MR-1. In a lactate medium, the composite electrode achieved a maximum current output of 1.5 A/m^2 over a constant load of $2 \text{ k}\Omega$. SEM images of the electrode taken ~ 30 days after inoculation revealed internal colonization⁶⁸. In another study, Wang et al. prepared a 3D scaffold of polyacrylonitrile/graphite composite by using supercritical CO_2 as a physical foaming agent (Figure 15). The composite was then subject to carbonization⁶¹. The electrode was tested in a MFC seeded with *E. coli* and fed glucose. From a polarization measurement, the authors reported a maximum current density of 2.91 A/m^2 , or 2.91 kA/m^3 . SEM images showed that biofilm was on both the surface and the cellular wall of the electrode, but the pore size of the electrode was only $0.5\text{-}5 \mu\text{m}$, insufficiently large for long-term biofilm growth without clogging.

2.4.6 Electrodes prepared by solvent cast and particulate leaching

Luckarift et al. manufactured a polymer/carbon 3D composite bioelectrode through a solvent cast and particulate leaching process (Figure 16A)⁷³. Graphitized carbon nanofibers ($0.5\text{-}20 \mu\text{m}$ long) and wet sucrose particles ($250\text{-}595 \mu\text{m}$) were mixed with weight ratio of 1:100, then filled into a mold. After overnight drying at $37 \text{ }^\circ\text{C}$, the composite was soaked with a chloroform solution containing 0.04% of poly 3-hydroxybutyrate-co-3-hydroxyvalerate (PHBV). After overnight drying a second time, this time at $25 \text{ }^\circ\text{C}$, the composite was immersed in to deionized water for 2 h, and the sucrose dissolved, leaving macroscale pores with size of several hundred μm (Figure

16B). The resulting composite electrode had 3D PHBV scaffolds with an open porous structure. The authors tested sucrose particles of differing size and found out that particle size was critical: if the particles were too small, the PHBV could not fill the gaps; if they were too large, the scaffold was poorly interconnected and mechanically brittle. The embedded carbon nanofibers distributed homogeneously and formed a conductive matrix for charge collection. However the conductivity of the composite was less than plain carbon nanofibers due to incorporation of nonconductive PHBV. The composite electrode (diameter, 1.3 cm; height, 0.9 cm; volume, 1.195 cm³) was evaluated as an anode in a lactate-fed MFCs. According to polarization measurements, the maximum current density achieved was 22.18±6.69 A/m³. In this work, *S. oneidensis* DSP-10 was harvested from a culture solution and directly immobilized on the anode surface via silica encapsulation (Scheme 2K). It was not clear whether internal colonization could be achieved by natural inoculation. The authors only showed 8 h of operation. The long-term integrity of this electrode in wastewater treatment applications is likely problematic given that PHBV is a desirable carbon source for microbial growth.

2.4.7 Electrodes prepared by ice segregation induced self-assembly

Katuri et al. fabricated a MWCNT/chitosan 3D composite bioelectrode by ice segregation induced self-assembly (ISISA) followed by freeze-drying (Figure 17A)⁷⁵. Functionalized MWCNTs were suspended in an acetic acid solution (0.05 M) containing chitosan (1% w/v). Syringes filled with this suspension were dipped into a cold bath (-196 °C) gradually. After freeze-drying, the solvent was removed, resulting in a conductive 3D scaffold that contains 89% MWCNTs and 11% chitosan. Micro-channels with an average size of 16 μm formed due to unidirectional freezing. The immersion rate

during this process determines the pore size of the micro-channels (Figure 17B-D). The authors estimated that the total surface area available for microbial colonization (315 cm^2) was 270 times that of the projected geometrical surface area (1.17 cm^2) of a cylindrical composite electrode (diameter, 0.45 cm; height, 0.9 cm; volume, 0.143 cm^3). The resulting composite electrode was used as an anode in a MFC, with an acetate solution continuously circulated through the anode at a flow rate of 12 mL/h. For this flow-through mode, metabolically active *G. sulfurreducens* colonized the internal surface of the 3D anode (Scheme 2L), as confirmed by both SEM (Figure 17E) and confocal laser scanning microscopy (Figure 17F). Only sub-monolayer of biofilm formed probably due to the peeling effect of the flowing media. A maximum current density of 24.5 A/m^2 , or 19 kA/m^3 , was achieved after polarization of the anode at 0 V vs. Ag/AgCl for 200 h. No internal colonization and lower maximum current density (10.8 A/m^2 , or 8.4 kA/m^3) resulted when the same anode was operated in batch-fed mode.

By replacing the MWCNTs with vacuum-stripped graphene (VSG), He et al. applied the same ISISA technique and prepared a 3D VSG/chitosan composite electrode (Figure 17G)⁷⁶. Chitosan created a supporting scaffold with layered structure, while the embedded VSG made the composite conductive. They characterized the VSG/chitosan composite with different weight ratios, and found that a more branched structure, with cross-linking of the layers into a network, occurred with higher VSG composition, but too much VSG (>70 wt %) disrupted layer structure and did not improve conductivity. The optimized composite had 50 wt% VSG. The spacing between layers was 30-50 μm . This spacing was mainly dependent upon the dipping rate during nitrogen freezing and/or chitosan concentration. The VSG/chitosan composite electrode was evaluated in a MFC

containing glucose-fed *P. aeruginosa* in the anode and potassium hexacyanoferrate ($\text{K}_3\text{Fe}(\text{CN})_6$) at the cathode. With a constant load of 1.96 k Ω , the anode achieved a maximum current output of 2.55 A/m², based on the lateral area of the cylindrical anode, but the exact size of the anode was not indicated. SEM images indicated formation of thick biofilms in the macroscale pores without clogging (Figure 17H), but the operating period before imaging was not indicated. The current profile for this MFC showed data for 300 h of operation.

Chen et al. prepared a macroporous flexible 3D electrode with only reduced graphene by ISISA⁷⁷. During ice segregation, graphene nanosheets were repelled by ice crystals and stacked into several- μm -thick highly ordered layers with lateral distance of 100-500 μm . This graphene sponge electrode was evaluated as an anode in a two-chamber MFC seeded with wastewater and fed acetate. With a constant load of 1 k Ω , the anode achieved a maximum current output of ~ 3 kA/m³. SEM images were taken after one month of operation. Biofilms were present throughout the cross-section of the electrode, but cell density decreased at locations closer to the inner space, in part due to microporous structure that was inaccessible for microbes, such as closed pores. These findings indicate insufficient mass transfer for internal colonization.

In another study, Massazza et al. applied ISISA to make TiO₂ porous scaffolds⁶². Subsequently, TiO₂ was reduced to conductive Ti₄O₇ by Zr under 1000 °C, forming 3D electrodes. These electrodes were polarized at 0.2 V vs Ag/AgCl in an acetate medium inoculated with *G. sulfurreducens*. The current output reached 128.7 A/m² or 9.5 kA/m³ over a 200 h period of operation. Although high current densities were achieved, long-

term performance of the electrode remains unclear. The channel size was only 10-15 μm , a length scale that could easily be clogged by biofilms.

3. “Best practices” for bioelectrode characterization

Several researchers have reported Brunauer–Emmett–Teller (BET) surface areas for new porous electrodes^{165, 166}. BET is based upon nitrogen absorption and desorption, and the surface area measurements obtained include surfaces within pores at the nm scale. Knowledge of surface area at the nm to μm scale may have some value as an indirect metric of surface roughness and potential for microbial attachment and electron transfer, but pores accessed by BET are not accessed by exoelectrogens and are likely to be covered or clogged by biofilms. Bioelectrodes containing only nm to μm scale pores are thus similar to the nonporous bulk electrodes described previously.

SEM and other imaging techniques provide the most direct and useful insight into the pore scale of new BES bioelectrodes. Images taken before and after colonization are needed. At present, many papers show images of porous electrodes before colonization, or images of a small area of microorganism-covered electrode surface at high magnification, making it difficult to discern how biofilm operation is affecting porosity. An additional concern is that bioelectrodes are only operated for a few days, preventing insight into long-term clogging issues. A final concern is that most bioelectrodes are tested in a synthetic electrolyte without suspended particles. In practical applications, the electrolyte can be much more turbid, a situation that may exacerbate clogging.

When reporting the performance of new bioelectrodes for BESs, many current studies currently report power density, a parameter that is highly affected by the counter electrodes used. To characterize the bioelectrodes and enable comparison with other studies, more attention should be paid to current densities and potential drops at the bioelectrodes. Polarization curves give both current densities and potential losses, but may not be sustainable during long-term operation. There is a critical need for long-term studies that report current density during operation.

4. Summary

Porous electrodes typically outperform nonporous electrodes due to their increased surface area and improved contact between microorganisms and the electrode surface (Table 4). Design of bioelectrodes is fundamentally different from the design of conventional porous electrode used in abiotic electrochemical systems. Bioelectrodes require consideration of the thermodynamic properties, including allowance for microbial energy requirements, and larger pores are needed to enable substrate delivery and removal of products. Many electrodes currently marketed as BESs and described as “porous” are in fact not porous at the scale required for effective microbial activity. Only a few of the current bioelectrode designs have demonstrated potential as microbial habitats that are sustainable without clogging in long-term operation. Demonstrated 3D porous bioelectrodes include packed bed electrodes, stainless steel mesh, carbon felt, carbon brush, CNT-textile, and most of the monolithic porous electrodes (Scheme 2).

For 3D packed bed bioelectrodes, granular electrode materials are usually cheap, but the granules need to be tightly packed to ensure that the entire bed is conductive.

Close packing results in decreased porosities, and inefficient utilization of reactor volume. Moreover, close packed structures can still be clogged without sufficient flushing. In long-term operation, clogging creates dead zones where substrate delivery is limited and current collection is low.

Stainless steel mesh has several advantages including low cost, high conductivity, superior mechanical properties, and the potential for creation of pores over size ranges that are tunable from tens of μm to tens of mm. As a surface for microbial growth, however, stainless steel is not attractive, and surface modifications are needed to improve its capacity to support growth and extracellular electron transfer. Depending upon the quality of the steel, the stability of the electrode in a BES may be of concern.

Carbon felt and the CNT-textile electrode both have 3D open porous structures, but the spacing of electrodes is not uniform. In addition, the contact between conductive fibers can be interrupted during operation, resulting in an increase in internal resistance. Carbon brush electrodes use a center metal wire that improves electrical contact to graphite fibers, but the spacing between fibers is also not uniform and the size of the brush is limited due to the brittleness of graphite fibers.

Monolithic porous electrodes show the most promise for practical application of BESs, because of their open 3D interconnected framework, strong mechanical support, and potential for uniformly distributed and tunable microbially-accessible pores and conductive electron pathways. To date, monolithic porous electrodes have achieved the highest current density of all bioelectrodes evaluated. For large scale BES applications, such as wastewater treatment with MFCs, however, cost may still be a concern, because

most of the monolithic porous electrodes described to date use expensive materials, such as CNTs, or require complex and energy-consuming synthetic steps, such as carbonization or freezing. Development of cost-effective porous electrodes is a high priority.

Acknowledgement

Xing Xie acknowledges support from a Stanford Interdisciplinary Graduate Fellowship.

References

1. B. E. Logan, *Nature Reviews Microbiology*, 2009, 7, 375-381.
2. B. E. Logan and K. Rabaey, *Science*, 2012, 337, 686-690.
3. D. R. Lovley, *Nature Reviews Microbiology*, 2006, 4, 497-508.
4. K. Rabaey and R. A. Rozendal, *Nature Reviews Microbiology*, 2010, 8, 706-716.
5. B. E. Rittmann, R. Krajmalnik-Brown and R. U. Halden, *Nature Reviews Microbiology*, 2008, 6, 604-612.
6. J. B. A. Arends and W. Verstraete, *Microbial Biotechnology*, 2012, 5, 333-346.
7. U. Schröder, F. Harnisch and L. T. Angenent, *Energy & Environmental Science*, 2015, 8, 513-519.
8. Y.-C. Yong, X.-C. Dong, M. B. Chan-Park, H. Song and P. Chen, *Acs Nano*, 2012, 6, 2394-2400.
9. H. Richter, K. McCarthy, K. P. Nevin, J. P. Johnson, V. M. Rotello and D. R. Lovley, *Langmuir*, 2008, 24, 4376-4379.
10. Y. Wang, B. Li, L. Zeng, D. Cui, X. Xiang and W. Li, *Biosensors & Bioelectronics*, 2013, 41, 582-588.
11. D. Xing, Y. Zuo, S. Cheng, J. M. Regan and B. E. Logan, *Environmental Science & Technology*, 2008, 42, 4146-4151.
12. Y. Zuo, D. Xing, J. M. Regan and B. E. Logan, *Applied and Environmental Microbiology*, 2008, 74, 3130-3137.
13. M. C. Potter, *Proceedings of the Royal Society of London*, 1911, 84, 260-276.
14. J. B. Davis and J. H. F. Yarbrough, *Science*, 1962, 137, 615-616.
15. J. J. Konikoff, L. W. Reynolds and E. S. Harris, *Aerospace Medicine*, 1963, 34, 1129-1133.
16. H. P. Bennetto, J. L. Stirling, K. Tanaka and C. A. Vega, *Biotechnology and Bioengineering*, 1983, 25, 559-568.
17. C. E. Reimers, L. M. Tender, S. Fertig and W. Wang, *Environmental Science & Technology*, 2001, 35, 192-195.
18. H. J. Kim, H. S. Park, M. S. Hyun, I. S. Chang, M. Kim and B. H. Kim, *Enzyme and Microbial Technology*, 2002, 30, 145-152.

19. H. Liu, R. Ramnarayanan and B. E. Logan, *Environmental Science & Technology*, 2004, 38, 2281-2285.
20. H. Liu, S. Grot and B. E. Logan, *Environmental Science & Technology*, 2005, 39, 4317-4320.
21. G. Reguera, K. D. McCarthy, T. Mehta, J. S. Nicoll, M. T. Tuominen and D. R. Lovley, *Nature*, 2005, 435, 1098-1101.
22. B. Logan, S. Cheng, V. Watson and G. Estadt, *Environmental Science & Technology*, 2007, 41, 3341-3346.
23. X. Xie, L. Hu, M. Pasta, G. F. Wells, D. Kong, C. S. Criddle and Y. Cui, *Nano Letters*, 2011, 11, 291-296.
24. X. Xie, M. Ye, P.-C. Hsu, N. Liu, C. S. Criddle and Y. Cui, *Proceedings of the National Academy of Sciences of the United States of America*, 2013, 110, 15925-15930.
25. E. Marsili, D. B. Baron, I. D. Shikhare, D. Coursolle, J. A. Gralnick and D. R. Bond, *Proceedings of the National Academy of Sciences of the United States of America*, 2008, 105, 3968-3973.
26. Y. A. Gorby, S. Yanina, J. S. McLean, K. M. Rosso, D. Moyles, A. Dohnalkova, T. J. Beveridge, I. S. Chang, B. H. Kim, K. S. Kim, D. E. Culley, S. B. Reed, M. F. Romine, D. A. Saffarini, E. A. Hill, L. Shi, D. A. Elias, D. W. Kennedy, G. Pinchuk, K. Watanabe, S. Ishii, B. Logan, K. H. Nealson and J. K. Fredrickson, *Proceedings of the National Academy of Sciences of the United States of America*, 2006, 103, 11358-11363.
27. S. E. Childers, S. Ciufu and D. R. Lovley, *Nature*, 2002, 416, 767-769.
28. International Patent WO 2001004061 A1, 2001.
29. D. Sell, P. Krämer and G. Kreysa, *Applied Microbiology and Biotechnology*, 1989, 31, 211-213.
30. J. B. Davis, *Advances in applied microbiology*, 1963, 5, 51-64.
31. S. Chen, H. Hou, F. Harnisch, S. A. Patil, A. A. Carmona-Martinez, S. Agarwal, Y. Zhang, S. Sinha-Ray, A. L. Yarin, A. Greiner and U. Schröder, *Energy & Environmental Science*, 2011, 4, 1417-1421.
32. D. R. Bond, D. E. Holmes, L. M. Tender and D. R. Lovley, *Science*, 2002, 295, 483-485.
33. L. M. Tender, C. E. Reimers, H. A. Stecher, D. E. Holmes, D. R. Bond, D. A. Lowy, K. Pilobello, S. J. Fertig and D. R. Lovley, *Nature Biotechnology*, 2002, 20, 821-825.
34. S. K. Chaudhuri and D. R. Lovley, *Nature Biotechnology*, 2003, 21, 1229-1232.
35. X. Cao, X. Huang, P. Liang, K. Xiao, Y. Zhou, X. Zhang and B. E. Logan, *Environmental Science & Technology*, 2009, 43, 7148-7152.
36. C. Forrestal, P. Xu and Z. Ren, *Energy & Environmental Science*, 2012, 5, 7161-7167.
37. Y. Kim and B. E. Logan, *Environmental Science & Technology*, 2011, 45, 5834-5839.
38. R. D. Cusick, Y. Kim and B. E. Logan, *Science*, 2012, 335, 1474-1477.
39. S. W. Hong, Y. S. Choi, T. H. Chung, J. H. Song and H. S. Kim, *World Academy of Science, Engineering and Technology*, 2009, 54, 683-689.
40. Y. Yuan, S. Zhou and L. Zhuang, *Journal of Soils and Sediments*, 2010, 10, 1427-1433.
41. J. Cai and P. Zheng, *Bioresource Technology*, 2013, 128, 760-764.
42. C. S. Butler, P. Clauwaert, S. J. Green, W. Verstraete and R. Nerenberg, *Environmental Science & Technology*, 2010, 44, 4685-4691.
43. S. Cheng and B. E. Logan, *Proceedings of the National Academy of Sciences of the United States of America*, 2007, 104, 18871-18873.
44. L. Lu, N. Ren, X. Zhao, H. Wang, D. Wu and D. Xing, *Energy & Environmental Science*, 2011, 4, 1329-1336.
45. K. P. Nevin, S. A. Hensley, A. E. Franks, Z. M. Summers, J. H. Ou, T. L. Woodard, O. L. Snoeyenbos-West and D. R. Lovley, *Applied and Environmental Microbiology*, 2011, 77, 2882-2886.

46. T. Zhang, H. R. Nie, T. S. Bain, H. Y. Lu, M. M. Cui, O. L. Snoeyenbos-West, A. E. Franks, K. P. Nevin, T. P. Russell and D. R. Lovley, *Energy & Environmental Science*, 2013, 6, 217-224.
47. A. Kumlanghan, J. Liu, P. Thavarungkul, P. Kanatharana and B. Mattiasson, *Biosensors & Bioelectronics*, 2007, 22, 2939-2944.
48. S. Liang, J. Wenzhao, H. Changjun and L. Yu, *Biosensors & Bioelectronics*, 2011, 26, 1788-1799.
49. P. L. McCarty, J. Bae and J. Kim, *Environmental Science & Technology*, 2011, 45, 7100-7106.
50. X. Xie, M. Ye, L. Hu, N. Liu, J. R. McDonough, W. Chen, H. N. Alshareef, C. S. Criddle and Y. Cui, *Energy & Environmental Science*, 2012, 5, 5265-5270.
51. X. Xie, G. Yu, N. Liu, Z. Bao, C. S. Criddle and Y. Cui, *Energy & Environmental Science*, 2012, 5, 6862-6866.
52. B. E. Rittmann and P. L. McCarty, *Environmental Biotechnology: Principles and Applications*, McGraw-Hill Companies, Inc, New York, 2001.
53. M. Picot, L. Lapinsonniere, M. Rothballer and F. Barriere, *Biosensors & Bioelectronics*, 2011, 28, 181-188.
54. J. E. Mink, J. P. Rojas, B. E. Logan and M. M. Hussain, *Nano Letters*, 2012, 12, 791-795.
55. D. R. Lovley, in *Annual Review of Microbiology*, Vol 66, 2012, vol. 66, pp. 391-409.
56. S. Chen, G. He, X. Hu, M. Xie, S. Wang, D. Zeng, H. Hou and U. Schröder, *Chemsuschem*, 2012, 5, 1059-1063.
57. S. Chen, Q. Liu, G. He, Y. Zhou, M. Hanif, X. Peng, S. Wang and H. Hou, *Journal of Materials Chemistry*, 2012, 22, 18609-18613.
58. R. Karthikeyan, B. Wang, J. Xuan, J. W. C. Wong, P. K. H. Lee and M. K. H. Leung, *Electrochimica Acta*, 2015, 157, 314-323.
59. J. Li, J. Zhang, D. Ye, X. Zhu, Q. Liao and J. Zheng, *International Journal of Hydrogen Energy*, 2014, 39, 19242-19248.
60. J. Tang, Y. Yuan, T. Liu and S. Zhou, *Journal of Power Sources*, 2015, 274, 170-176.
61. Y.-Q. Wang, H.-X. Huang, B. Li and W.-S. Li, *Journal of Materials Chemistry A*, 2015, 3, 5110-5118.
62. D. Massazza, R. Parra, J. P. Busalmen and H. E. Romeo, *Energy & Environmental Science*, 2015, DOI: 10.1039/C5EE01498K.
63. S. S. Manickam, U. Karra, L. Huang, B. Nhu-Ngoc, B. Li and J. R. McCutcheon, *Carbon*, 2012, 53, 19-28.
64. S. Chen, G. He, Q. Liu, F. Harnisch, Y. Zhou, Y. Chen, M. Hanif, S. Wang, X. Peng, H. Hou and U. Schröder, *Energy & Environmental Science*, 2012, 5, 9769-9772.
65. Z. Wang, Z. Zheng, S. Zheng, S. Chen and F. Zhao, *Journal of Power Sources*, 2015, 287, 269-275.
66. G. Lepage, F. O. Albernaz, G. Perrier and G. Merlin, *Bioresource technology*, 2012, 124, 199-207.
67. B. R. Ringeisen, E. Henderson, P. K. Wu, J. Pietron, R. Ray, B. Little, J. C. Biffinger and J. M. Jones-Meehan, *Environmental Science & Technology*, 2006, 40, 2629-2634.
68. N. Tien-Hoa, Y.-Y. Yu, X. Wang, J.-Y. Wang and H. Song, *Chemical Communications*, 2013, 49, 10754-10756.
69. K. Rabaey, P. Clauwaert, P. Aelterman and W. Verstraete, *Environmental Science & Technology*, 2005, 39, 8077-8082.
70. P. Aelterman, M. Versichele, M. Marzorati, N. Boon and W. Verstraete, *Bioresource Technology*, 2008, 99, 8895-8902.
71. H. Wang, M. Davidson, Y. Zuo and Z. Ren, *Journal of Power Sources*, 2011, 196, 5863-5866.

72. B. Erable and A. Bergel, *Bioresource Technology*, 2009, 100, 3302-3307.
73. H. R. Luckarift, S. R. Sizemore, K. E. Farrington, J. Roy, C. Lau, P. B. Atanassov and G. R. Johnson, *ACS Applied Materials & Interfaces*, 2012, 4, 2082-2087.
74. Y. Feng, Q. Yang, X. Wang and B. E. Logan, *Journal of Power Sources*, 2010, 195, 1841-1844.
75. K. Katuri, M. Luisa Ferrer, M. C. Gutierrez, R. Jimenez, F. del Monte and D. Leech, *Energy & Environmental Science*, 2011, 4, 4201-4210.
76. Z. He, J. Liu, Y. Qiao, C. M. Li and T. T. Y. Tan, *Nano Letters*, 2012, 12, 4738-4741.
77. W. Chen, Y.-X. Huang, D.-B. Li, H.-Q. Yu and L. Yan, *Rsc Advances*, 2014, 4, 21619-21624.
78. Y. Shen, Y. Zhou, S. Chen, F. Yang, S. Zheng and H. Hou, *TheScientificWorldJournal*, 2014, 2014, 130185-130185.
79. Y. Zhao, K. Watanabe and K. Hashimoto, *Physical Chemistry Chemical Physics*, 2011, 13, 15016-15021.
80. Y. Zhao, K. Watanabe, R. Nakamura, S. Mori, H. Liu, K. Ishii and K. Hashimoto, *Chemistry-a European Journal*, 2010, 16, 4982-4985.
81. C. Feng, Z. Lv, X. Yang and C. Wei, *Physical Chemistry Chemical Physics*, 2014, 16, 10464-10472.
82. H.-F. Cui, L. Du, P.-B. Guo, B. Zhu and J. H. T. Luong, *Journal of Power Sources*, 2015, 283, 46-53.
83. X. Tang, H. Li, Z. Du, W. Wang and H. Y. Ng, *Rsc Advances*, 2015, 5, 50968-50974.
84. C. Zhang, P. Liang, Y. Jiang and X. Huang, *Journal of Power Sources*, 2015, 273, 580-583.
85. Z. Lv, D. Xie, X. Yue, C. Feng and C. Wei, *Journal of Power Sources*, 2012, 210, 26-31.
86. C. Li, L. Zhang, L. Ding, H. Ren and H. Cui, *Biosensors & Bioelectronics*, 2011, 26, 4169-4176.
87. M. Adachi, T. Shimomura, M. Komatsu, H. Yakuwa and A. Miya, *Chemical Communications*, 2008, 2055-2057.
88. B. Cercado-Quezada, M.-L. Delia and A. Bergel, *Electrochemistry Communications*, 2011, 13, 440-443.
89. V. Flexer, J. Chen, B. C. Donose, P. Sherrell, G. G. Wallace and J. Keller, *Energy & Environmental Science*, 2013, 6, 1291-1298.
90. C. Erbay, X. Pu, W. Choi, M.-J. Choi, Y. Ryu, H. Hou, F. Lin, P. de Figueiredo, C. Yu and A. Han, *Journal of Power Sources*, 2015, 280, 347-354.
91. J. Wei, P. Liang and X. Huang, *Bioresource Technology*, 2011, 102, 9335-9344.
92. M. Zhou, M. Chi, J. Luo, H. He and T. Jin, *Journal of Power Sources*, 2011, 196, 4427-4435.
93. G. G. Kumar, V. G. S. Sarathi and K. S. Nahm, *Biosensors & Bioelectronics*, 2013, 43, 461-475.
94. A. Baudler, I. Schmidt, M. Langner, A. Greiner and U. Schröder, *Energy & Environmental Science*, 2015, 8, 2048-2055.
95. C. I. Torres, A. K. Marcus and B. E. Rittmann, *Biotechnology and Bioengineering*, 2008, 100, 872-881.
96. L. Peng, S.-J. You and J.-Y. Wang, *Biosensors & Bioelectronics*, 2010, 25, 1248-1251.
97. A. Mehdinia, E. Ziaei and A. Jabbari, *Electrochimica Acta*, 2014, 130, 512-518.
98. Y. Fu, J. Yu, Y. Zhang and Y. Meng, *Applied Surface Science*, 2014, 317, 84-89.
99. J. Tang, S. Chen, Y. Yuan, X. Cai and S. Zhou, *Biosensors & Bioelectronics*, 2015, 71, 387-395.
100. Y. Fan, S. Xu, R. Schaller, J. Jiao, F. Chaplen and H. Liu, *Biosensors & Bioelectronics*, 2011, 26, 1908-1912.

101. D. A. Lowy, L. M. Tender, J. G. Zeikus, D. H. Park and D. R. Lovley, *Biosensors & Bioelectronics*, 2006, 21, 2058-2063.
102. A. Mehdinia, M. Dejaloud and A. Jabbari, *Chemical Papers*, 2013, 67, 1096-1102.
103. Y. Fu, Z. Zhao, J. Liu, K. Li, Q. Xu and S. Zhang, *Science China-Chemistry*, 2011, 54, 844-849.
104. A. Deeke, T. H. J. A. Sleutels, H. V. M. Hamelers and C. J. N. Buisman, *Environmental Science & Technology*, 2012, 46, 3554-3560.
105. S. R. Crittenden, C. J. Sund and J. J. Sumner, *Langmuir*, 2006, 22, 9473-9476.
106. Y. Liu, H. Kim, R. Franklin and D. R. Bond, *Energy & Environmental Science*, 2010, 3, 1782-1788.
107. A. ter Heijne, H. V. M. Hamelers, M. Saakes and C. J. N. Buisman, *Electrochimica Acta*, 2008, 53, 5697-5703.
108. C. Dumas, R. Basseguy and A. Bergel, *Electrochimica Acta*, 2008, 53, 5235-5241.
109. C. Dumas, A. Mollica, D. Feron, R. Basseguy, L. Etcheverry and A. Bergel, *Electrochimica Acta*, 2007, 53, 468-473.
110. T. Zhang, C. Z. Cui, S. L. Chen, X. P. Ai, H. X. Yang, S. Ping and Z. R. Peng, *Chemical Communications*, 2006, 2257-2259.
111. T. Zhang, Y. Zeng, S. Chen, X. Ai and H. Yang, *Electrochemistry Communications*, 2007, 9, 349-353.
112. Y. Zhang, G. Mo, X. Li, W. Zhang, J. Zhang, J. Ye, X. Huang and C. Yu, *Journal of Power Sources*, 2011, 196, 5402-5407.
113. X. Peng, H. Yu, X. Wang, N. Gao, L. Geng and L. Ai, *Journal of Power Sources*, 2013, 223, 94-99.
114. Y. Wang, B. Li, D. Cui, X. Xiang and W. Li, *Biosensors & Bioelectronics*, 2014, 51, 349-355.
115. Y. Qiao, S.-J. Bao, C. M. Li, X.-Q. Cui, Z.-S. Lu and J. Guo, *Acs Nano*, 2008, 2, 113-119.
116. Y. Qiao, C. M. Li, S.-J. Bao and Q.-L. Bao, *Journal of Power Sources*, 2007, 170, 79-84.
117. C.-e. Zhao, W.-J. Wang, D. Sun, X. Wang, J.-R. Zhang and J.-J. Zhu, *Chemistry-a European Journal*, 2014, 20, 7091-7097.
118. Y. Yuan, S. Zhou, N. Xu and L. Zhuang, *Applied Microbiology and Biotechnology*, 2011, 89, 1629-1635.
119. J. S. Cho, J. Y. Park and Y. J. Yoo, *Biotechnology Letters*, 2008, 30, 1617-1620.
120. P. Liang, H. Wang, X. Xia, X. Huang, Y. Mo, X. Cao and M. Fan, *Biosensors & Bioelectronics*, 2011, 26, 3000-3004.
121. Y. Yuan, S. Zhou, B. Zhao, L. Zhuang and Y. Wang, *Bioresource Technology*, 2012, 116, 453-458.
122. I. H. Park, M. Christy, P. Kim and K. S. Nahm, *Biosensors & Bioelectronics*, 2014, 58, 75-80.
123. M. Di Lorenzo, K. Scott, T. P. Curtis and I. M. Head, *Chemical Engineering Journal*, 2010, 156, 40-48.
124. D. Q. Jiang and B. K. Li, *Biochemical Engineering Journal*, 2009, 47, 31-37.
125. F. Li, Y. Sharma, Y. Lei, B. Li and Q. Zhou, *Applied Biochemistry and Biotechnology*, 2010, 160, 168-181.
126. T. Sharma, A. L. M. Reddy, T. S. Chandra and S. Ramaprabhu, *International Journal of Hydrogen Energy*, 2008, 33, 6749-6754.
127. Y. J. Zou, C. L. Xiang, L. N. Yang, L. X. Sun, F. Xu and Z. Cao, *International Journal of Hydrogen Energy*, 2008, 33, 4856-4862.
128. C.-e. Zhao, P. Gai, R. Song, J. Zhang and J.-J. Zhu, *Analytical Methods*, 2015, 7, 4640-4644.

129. Y.-R. He, X. Xiao, W.-W. Li, G.-P. Sheng, F.-F. Yan, H.-Q. Yu, H. Yuan and L.-J. Wu, *Physical Chemistry Chemical Physics*, 2012, 14, 9966-9971.
130. Y. Zhang, J. Sun, B. Hou and Y. Hu, *Journal of Power Sources*, 2011, 196, 7458-7464.
131. W. Guo, Y. Cui, H. Song and J. Sun, *Bioprocess and Biosystems Engineering*, 2014, 37, 1749-1758.
132. X.-W. Liu, J.-J. Chen, Y.-X. Huang, X.-F. Sun, G.-P. Sheng, D.-B. Li, L. Xiong, Y.-Y. Zhang, F. Zhao and H.-Q. Yu, *Scientific Reports*, 2014, 4.
133. X.-W. Liu, X.-F. Sun, Y.-X. Huang, G.-P. Sheng, S.-G. Wang and H.-Q. Yu, *Energy & Environmental Science*, 2011, 4, 1422-1427.
134. X.-W. Liu, Y.-X. Huang, X.-F. Sun, G.-P. Sheng, F. Zhao, S.-G. Wang and H.-Q. Yu, *Acs Applied Materials & Interfaces*, 2014, 6, 8158-8164.
135. J. Hou, Z. Liu and P. Zhang, *Journal of Power Sources*, 2013, 224, 139-144.
136. B. Lai, X. Tang, H. Li, Z. Du, X. Liu and Q. Zhang, *Biosensors & Bioelectronics*, 2011, 28, 373-377.
137. D. Jiang and B. Li, *Water Science and Technology*, 2009, 59, 557-563.
138. H. Y. Tsai, C. C. Wu, C. Y. Lee and E. P. Shih, *Journal of Power Sources*, 2009, 194, 199-205.
139. S. Ci, Z. Wen, J. Chen and Z. He, *Electrochemistry Communications*, 2012, 14, 71-74.
140. J. Liu, Y. Qiao, C. X. Guo, S. Lim, H. Song and C. M. Li, *Bioresource Technology*, 2012, 114, 275-280.
141. L. Xiao, J. Damien, J. Luo, H. D. Jang, J. Huang and Z. He, *Journal of Power Sources*, 2012, 208, 187-192.
142. A. Mehdinia, E. Ziaei and A. Jabbari, *International Journal of Hydrogen Energy*, 2014, 39, 10724-10730.
143. T. Saito, M. Mehanna, X. Wang, R. D. Cusick, Y. Feng, M. A. Hickner and B. E. Logan, *Bioresource Technology*, 2011, 102, 395-398.
144. B. Li, J. Zhou, X. Zhou, X. Wang, B. Li, C. Santoro, M. Grattieri, S. Babanova, K. Artyushkova, P. Atanassov and A. J. Schuler, *Electrochimica Acta*, 2014, 134, 116-126.
145. J. Liu, J. Liu, W. He, Y. Qu, N. Ren and Y. Feng, *Journal of Power Sources*, 2014, 265, 391-396.
146. J. Zhang, J. Li, D. Ye, X. Zhu, Q. Liao and B. Zhang, *International Journal of Hydrogen Energy*, 2014, 39, 19148-19155.
147. X. Liu, X. Du, X. Wang, N. Li, P. Xu and Y. Ding, *Biosensors & Bioelectronics*, 2012, 41, 848-851.
148. X. Wang, S. Cheng, Y. Feng, M. D. Merrill, T. Saito and B. E. Logan, *Environmental Science & Technology*, 2009, 43, 6870-6874.
149. M. Zhou, M. Chi, H. Wang and T. Jin, *Biochemical Engineering Journal*, 2012, 60, 151-155.
150. J. Luo, M. Chi, H. Wang, H. He and M. Zhou, *Bioprocess and Biosystems Engineering*, 2013, 36, 1889-1896.
151. J. L. Lamp, J. S. Guest, S. Naha, K. A. Radavich, N. G. Love, M. W. Ellis and I. K. Puri, *Journal of Power Sources*, 2011, 196, 5829-5834.
152. K. Scott, G. A. Rambu, K. P. Katuri, K. K. Prasad and I. M. Head, *Process Safety and Environmental Protection*, 2007, 85, 481-488.
153. X. Chen, D. Cui, X. Wang, X. Wang and W. Li, *Biosensors & Bioelectronics*, 2015, 69, 135-141.
154. Z. Lv, D. Xie, F. Li, Y. Hu, C. Wei and C. Feng, *Journal of Power Sources*, 2014, 246, 642-649.
155. United States Patent US5427871, 1995.

156. S. Chen, G. He, A. A. Carmona-Martinez, S. Agarwal, A. Greiner, H. Hou and U. Schröder, *Electrochemistry Communications*, 2011, 13, 1026-1029.
157. J. M. Friedrich, C. Ponce-De-Leon, G. W. Reade and F. C. Walsh, *Journal of Electroanalytical Chemistry*, 2004, 561, 203-217.
158. Z. He, S. D. Minter and L. T. Angenent, *Environmental Science & Technology*, 2005, 39, 5262-5267.
159. Y. Yuan and S. Kim, *Bulletin of the Korean Chemical Society*, 2008, 29, 168-172.
160. R. Thorne, H. Hu, K. Schneider, P. Bombelli, A. Fisher, L. M. Peter, A. Dent and P. J. Cameron, *Journal of Materials Chemistry*, 2011, 21, 18055-18060.
161. H. Wang, G. Wang, Y. Ling, F. Qian, Y. Song, X. Lu, S. Chen, Y. Tong and Y. Li, *Nanoscale*, 2013, 5, 10283-10290.
162. Y. Qiao, X.-S. Wu, C.-X. Ma, H. He and C. M. Li, *Rsc Advances*, 2014, 4, 21788-21793.
163. A. Baudler, S. Riedl and U. Schröder, *Frontiers in Energy Research*, 2014, 2, 30.
164. Y. Yuan, S. Zhou, Y. Liu and J. Tang, *Environmental Science & Technology*, 2013, 47, 14525-14532.
165. Y. Qiao, S. J. Bao, C. M. Li, X. Q. Cui, Z. S. Lu and J. Guo, *ACS Nano*, 2008, 2, 113-119.
166. Y. Qiao, C. M. Li, S. J. Bao and Q. L. Bao, *Journal of Power Sources*, 2007, 170, 79-84.

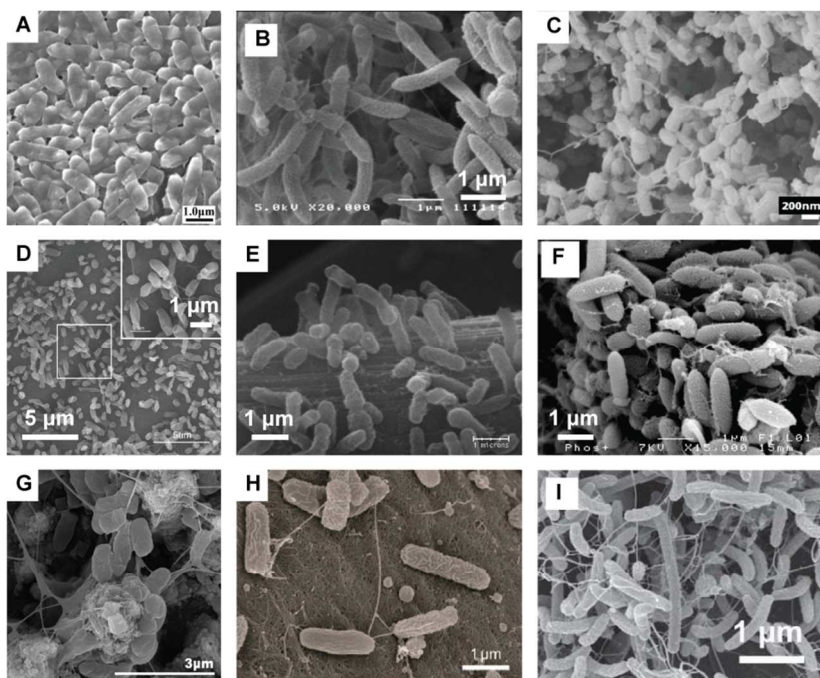


Figure 1. Scanning electron microscope (SEM) images of exoelectrogens. (A) *S. oneidensis* on a graphene/polyaniline composite electrode.⁸ (B) *G. sulfurreducens* on a gold electrode.⁹ (C) *E. coli* on a polyaniline/ WO_3 composite electrode.¹⁰ (D) *R. palustris* DX-1 on a carbon paper electrode.¹¹ (E) *O. anthropi* YZ-1 on a carbon cloth electrode.¹² (F) Mixed culture on a modified graphite electrode.⁵³ (G) Mixed culture on a multi-walled carbon nanotube (MWCNT) electrode.⁵⁴ (H) Mixed culture on a carbon nanotube (CNT)-coated textile electrode.²³ (I) Mixed culture on a graphene-coated sponge electrode.⁵¹ Reproduced with permission from American Chemical Society, American Society for Microbiology, and Elsevier.

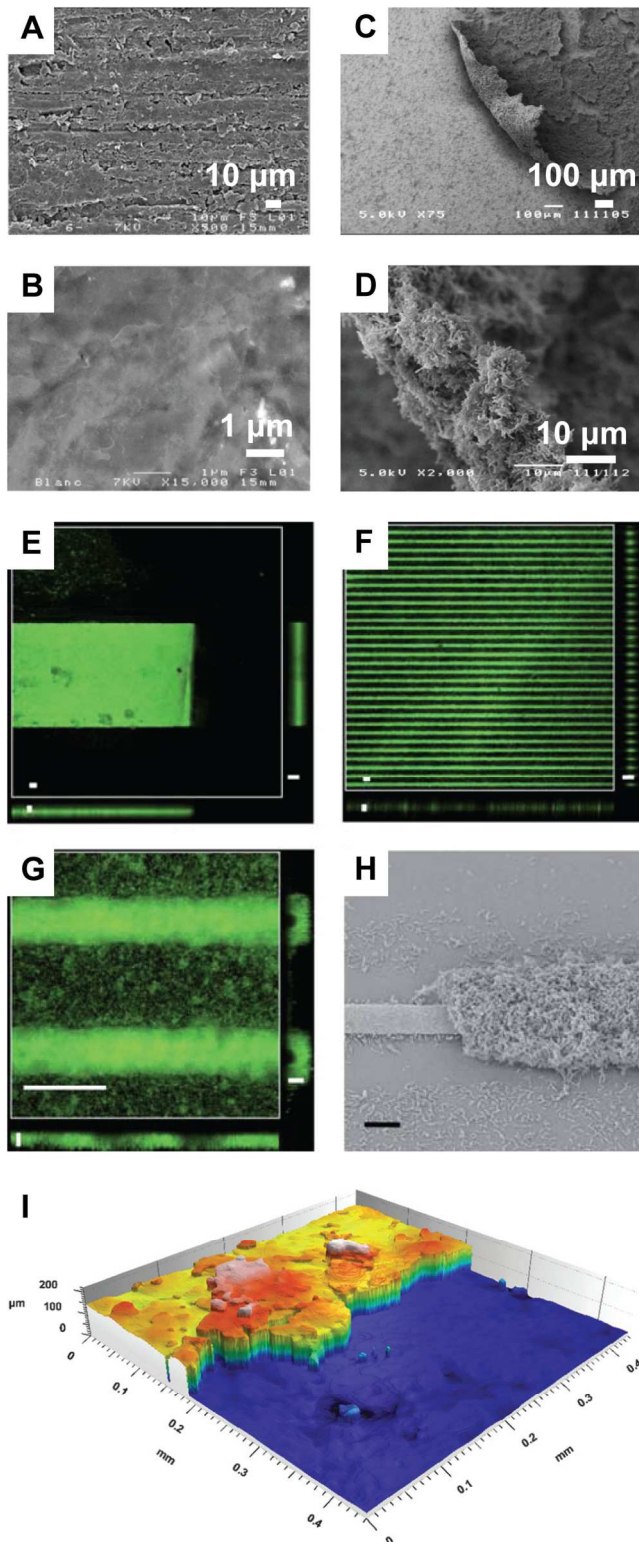


Figure 2. Nonporous bulk electrodes. (A, B) SEM images of pristine graphite surface.⁵³ (C, D) SEM images of biofilm attached to the surface of a gold electrode.⁹ (E-G) Confocal laser scanning microscopy images of gold rectangular electrode (E) and gold

line array electrode (F, G) after 140 h of colonization. The center images are maximum top projections of all slices in the 3-dimensional stack, the smaller images (bottom and right) are orthogonal cross-sections of the biofilm. Scale bars for top views in E and F are 100 μm , and side views are 50 μm . Top view scale bar in G is 100 μm , and side scale bars are 10 μm . (H) SEM image of a single line from the gold line array electrode. Scale bar is 10 μm .¹⁰⁶ (I) Confocal laser scanning microscopy image (reflectance data) of an anodic electrochemically active biofilm cultivated on a gold electrode.⁹⁴ Reproduced with permission from American Chemical Society and Elsevier.

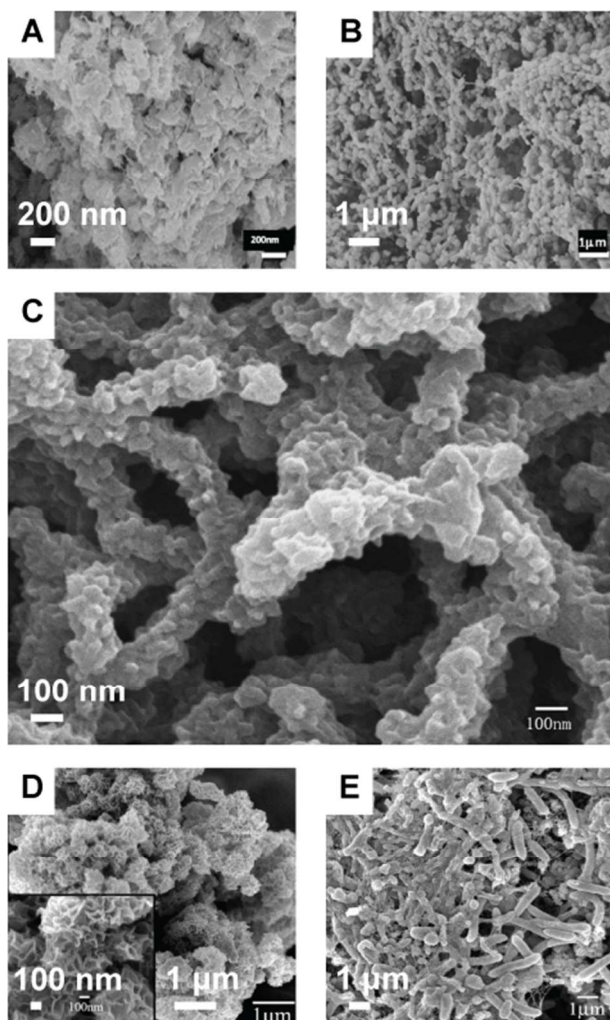


Figure 3. SEM images of densely piled electrodes. (A, B) Polyaniline/ WO_3 composite electrode before (A) and after (B) colonization.¹⁰ (C) Pristine CNT/Polyaniline composite electrode.¹¹⁶ (D, E) Polyaniline/ TiO_2 composite electrode before (D) and after (E) colonization.¹¹⁵ Reproduced with permission from American Chemical Society and Elsevier.

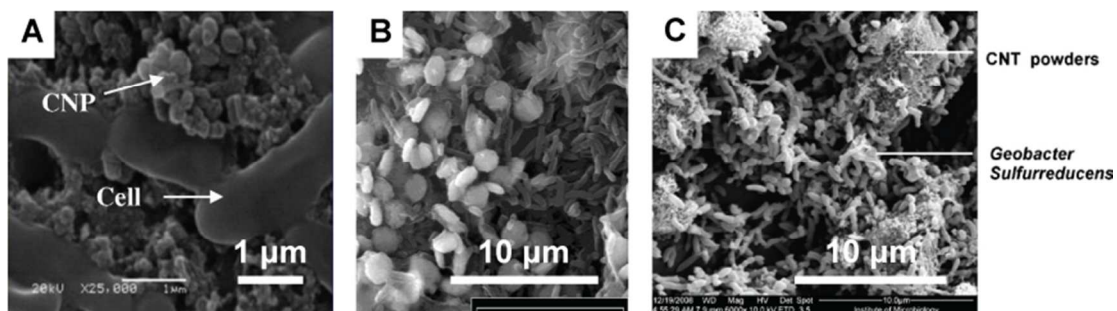


Figure 4. SEM images of cell-embedded electrodes. (A) Carbon nanoparticle mixed with anodic microorganisms from previous MFCs.¹¹⁸ (B) Copper particles (circular shape) mixed with permeabilized *Ochrobactrum anthropi* SY 509 cells (bar shape).¹¹⁹ (C) CNT powders mixed with *G. sulfurreducens*.¹²⁰ Reproduced with permission from Springer and Elsevier.

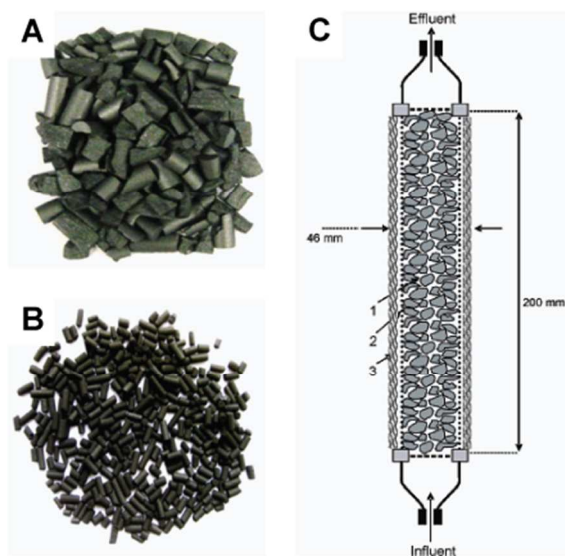


Figure 5. Packed bed electrodes. (A) Granular graphite. (B) Granular activated carbon.⁹¹ (C) Schematic of a tubular MFC filled with graphite granules (1, granular anode; 2, membrane; 3, cathode).⁶⁹ Reproduced with permission from American Chemical Society and Elsevier.

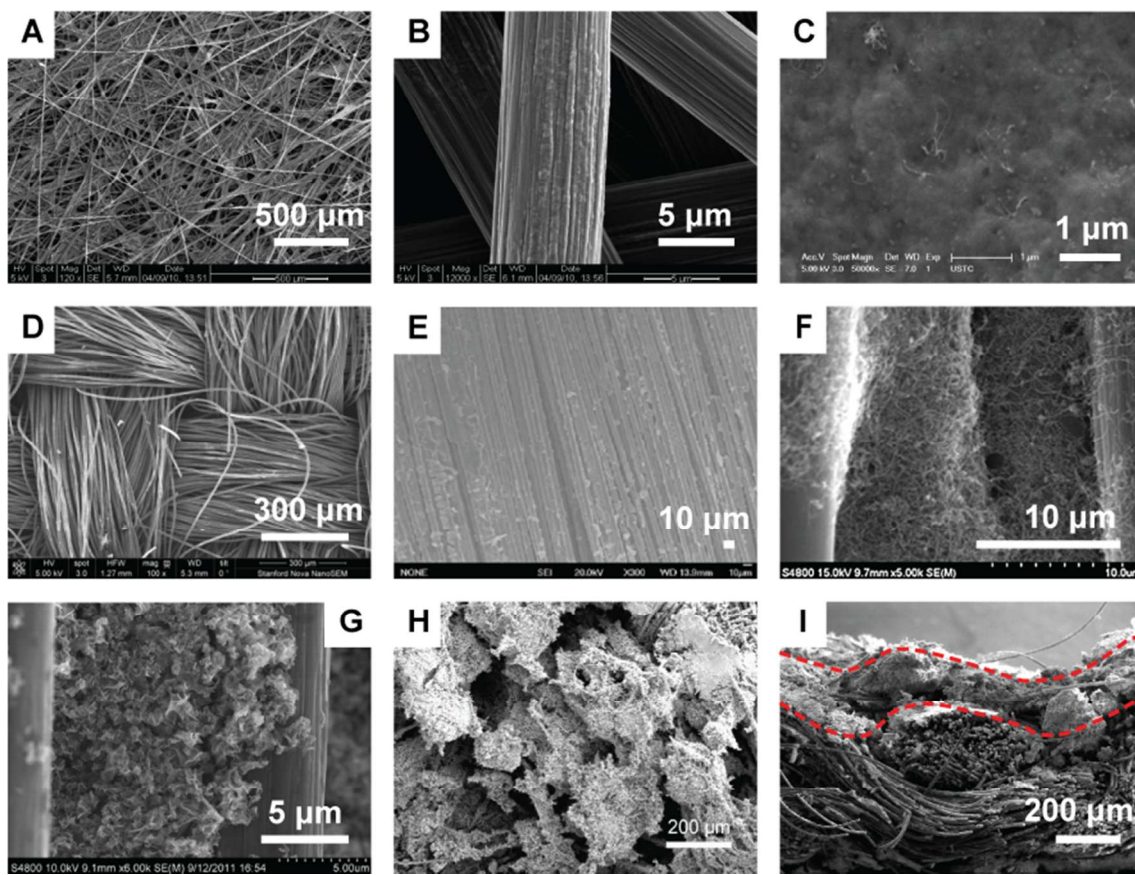


Figure 6. SEM images of planar porous carbon electrodes. (A, B) Unmodified carbon paper. (C) Carbon paper modified with CNT/Chitosan nanocomposite.¹³³ (D) Unmodified carbon cloth. (E) Polyaniline modified carbon cloth.¹³⁶ (F) Carbon cloth modified with MWCNTs.¹³⁸ (G) Carbon cloth modified with crumpled graphene particles.¹⁴¹ (H, I) Top view (H) and cross-section (I) of colonized a carbon cloth bioelectrode. The biofilm is limited to the outer surface (area between the two broken lines).²³ Reproduced with permission from American Chemical Society and Elsevier.

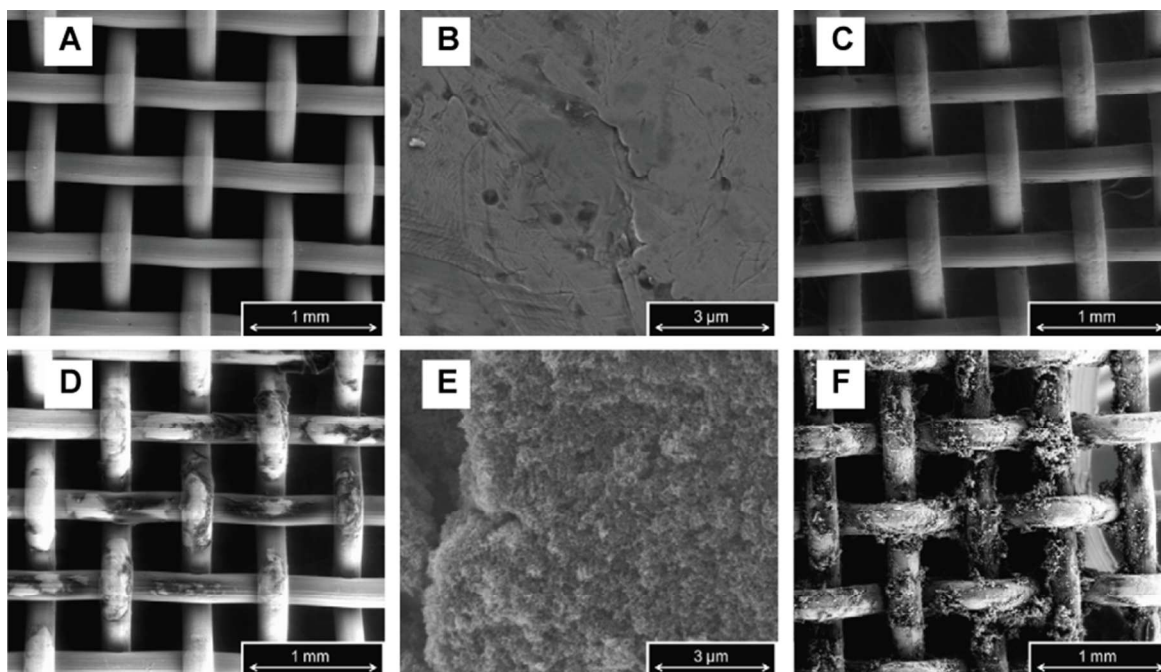


Figure 7. SEM images of stainless steel mesh electrodes. (A-C) Plain stainless steel mesh before (A, B) and after (C) inoculation. (D-F) Carbon nanostructure modified stainless steel mesh before (D, E) and after (F) inoculation. ¹⁵¹ Reproduced with permission from Elsevier.

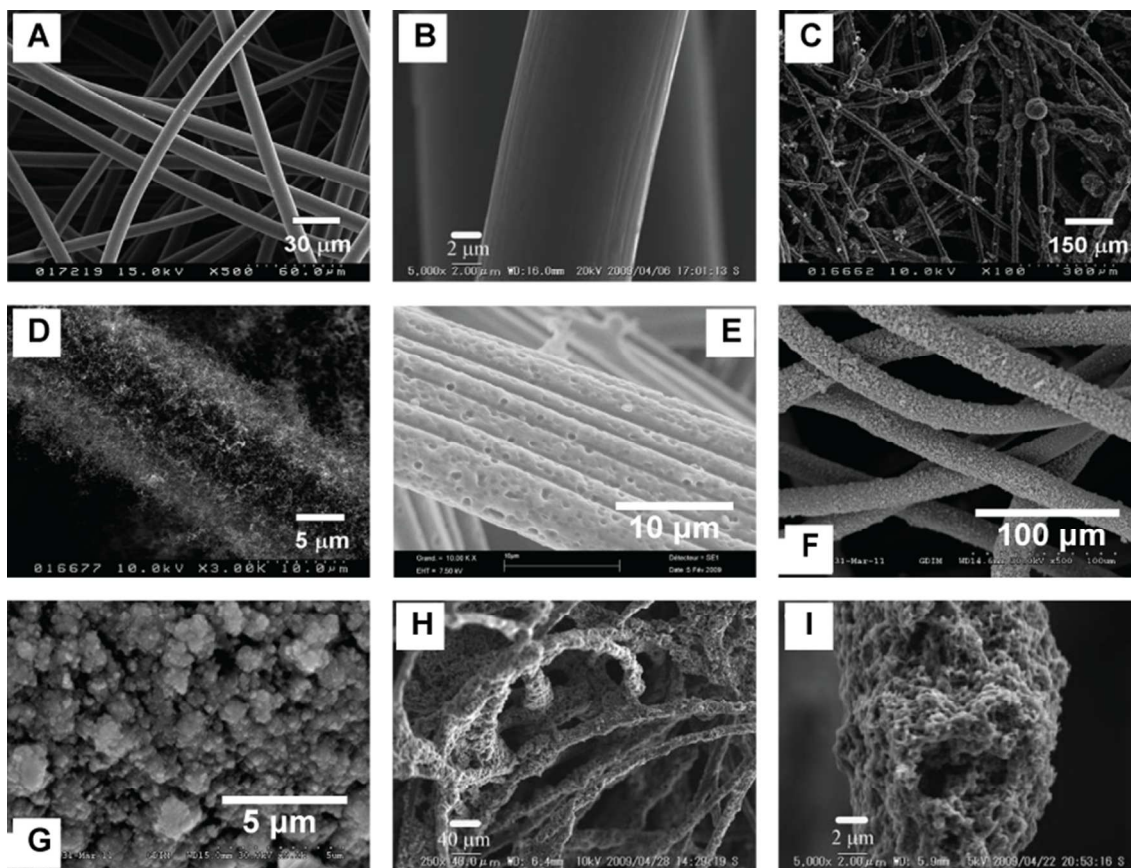


Figure 8. SEM images of carbon felt electrodes. (A, B) Bare carbon felt.^{79, 80} (C, D) CNT modified carbon felt.⁷⁹ (E) Carbon felt after anodisation.⁸⁸ (F, G) RuO₂ coated carbon felt.⁸⁵ (H, I) Carbon felt coated with polyaniline nanowire.⁸⁰ Reproduced with permission from Wiley and Elsevier.

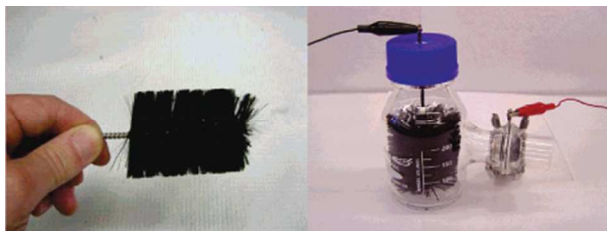


Figure 9. Carbon brush electrodes made from graphite fibers and titanium wires.²²
Reproduced with permission from American Chemical Society.

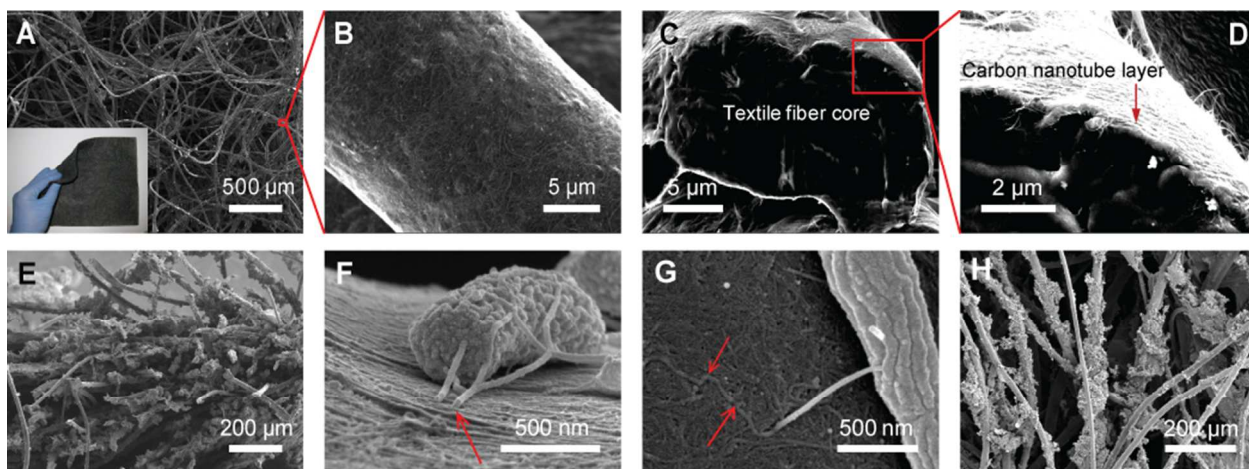


Figure 10. CNT coated textile electrodes. (A, B) CNT-textile as prepared. (C, D) Cross-section of a CNT-textile fiber. (E) Cross-section of a colonized CNT-textile bioelectrode. (F, G) Exoelectrogens on CNT-textile surface. The arrows in F and G indicate the microbial nanowires. (H) Colonized CNT-textile bioelectrode after 5 min of bath sonication and 10 s of vortex agitation.²³ Reproduced with permission from American Chemical Society.

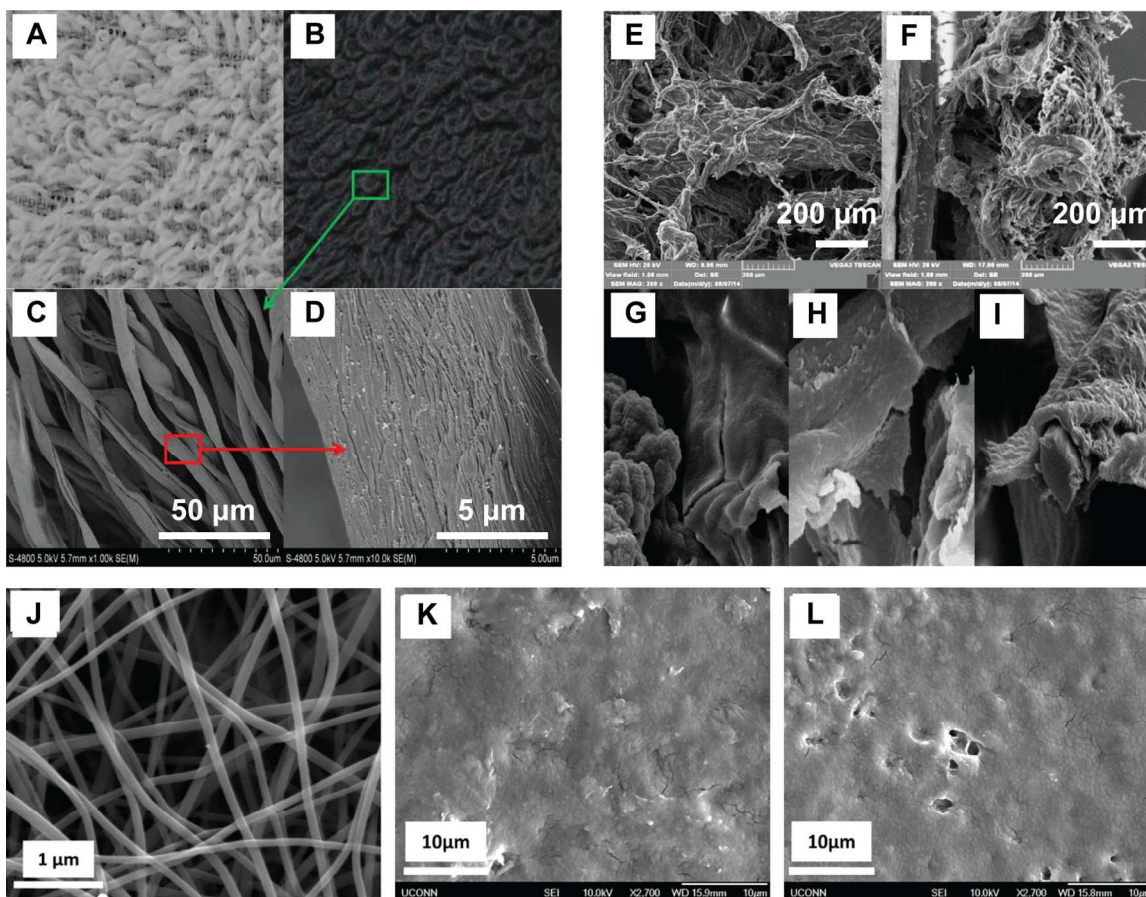


Figure 11. Carbonized textile/fiber electrodes. (A-I) Carbonized textile electrode. (A, B) Digital pictures of plain (A) and carbonized (B) textile. (C, D) SEM image of fiber (C) and fiber surface (D). (E-I) SEM images after colonization. (E, F) Front (E) and side-surface (F). (G-I) Fibers located at interior (G), middle (H) and external (I) part of the electrode substrate.⁶⁵ (J-L) Activated carbon nanofiber electrodes. (J) As prepared. (K) Colonized by *P. aeruginosa*. (L) Colonized by *S. oneidensis* MR-1.⁶³ Reproduced with permission from Elsevier.

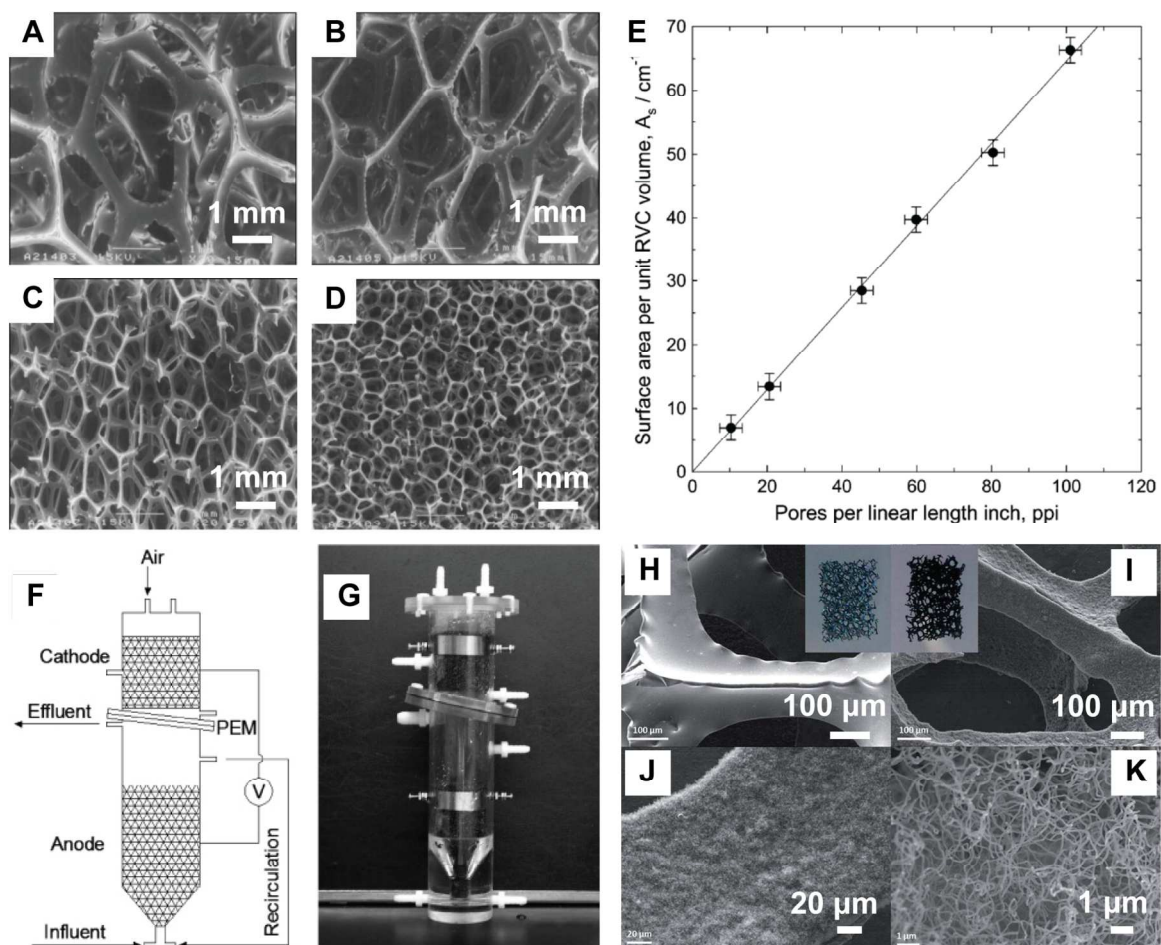


Figure 12. Reticulated vitreous carbon (RVC) electrodes. (A-D) SEM images of RVC with different PPI grades: (A) 10; (B) 30; (C) 60; (D) 100. (E) Electrode surface area of RVC with different PPI grades.¹⁵⁷ (F, G) Schematic (F) and physical image (G) of an upflow MFC equipped with RVC electrodes.¹⁵⁸ (H-K) SEM images of unmodified RVC (H) and CNTs modified RVC (I-K). Insets in (H) and (I) are photographic images.⁸⁹ Reproduced with permission from American Chemical Society and Elsevier.

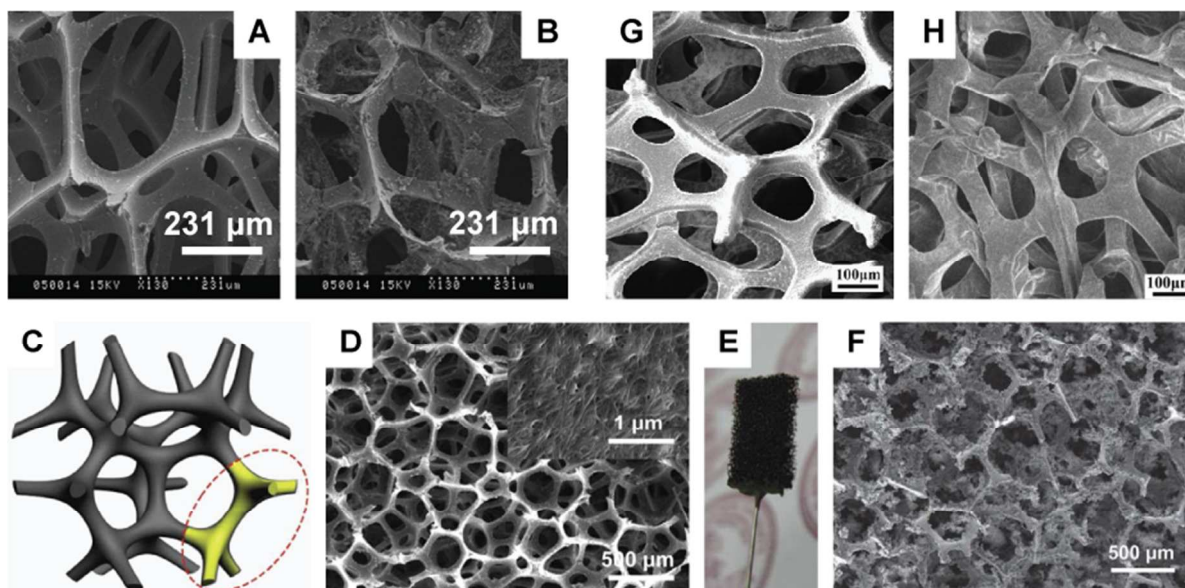


Figure 13. Sponge-templated electrodes. (A, B) SEM images of nickel coated sponge electrode before (A) and after (B) colonization.¹⁴⁷ (C-E) Schematic, SEM image, and physical image of CNT coated sponge electrode.⁵⁰ (F) Interior SEM image of the CNT-sponge bioelectrode after one year of operation.⁵⁰ (G) SEM image of three-dimensional (3D) graphene-sponge electrode fabricated by using a nickel foam template. (H) SEM image of the Polyaniline modified graphene sponge electrode after 60 h incubation in MFC with *S. oneidensis* MR-1.⁸ Reproduced with permission from American Chemical Society and Elsevier.

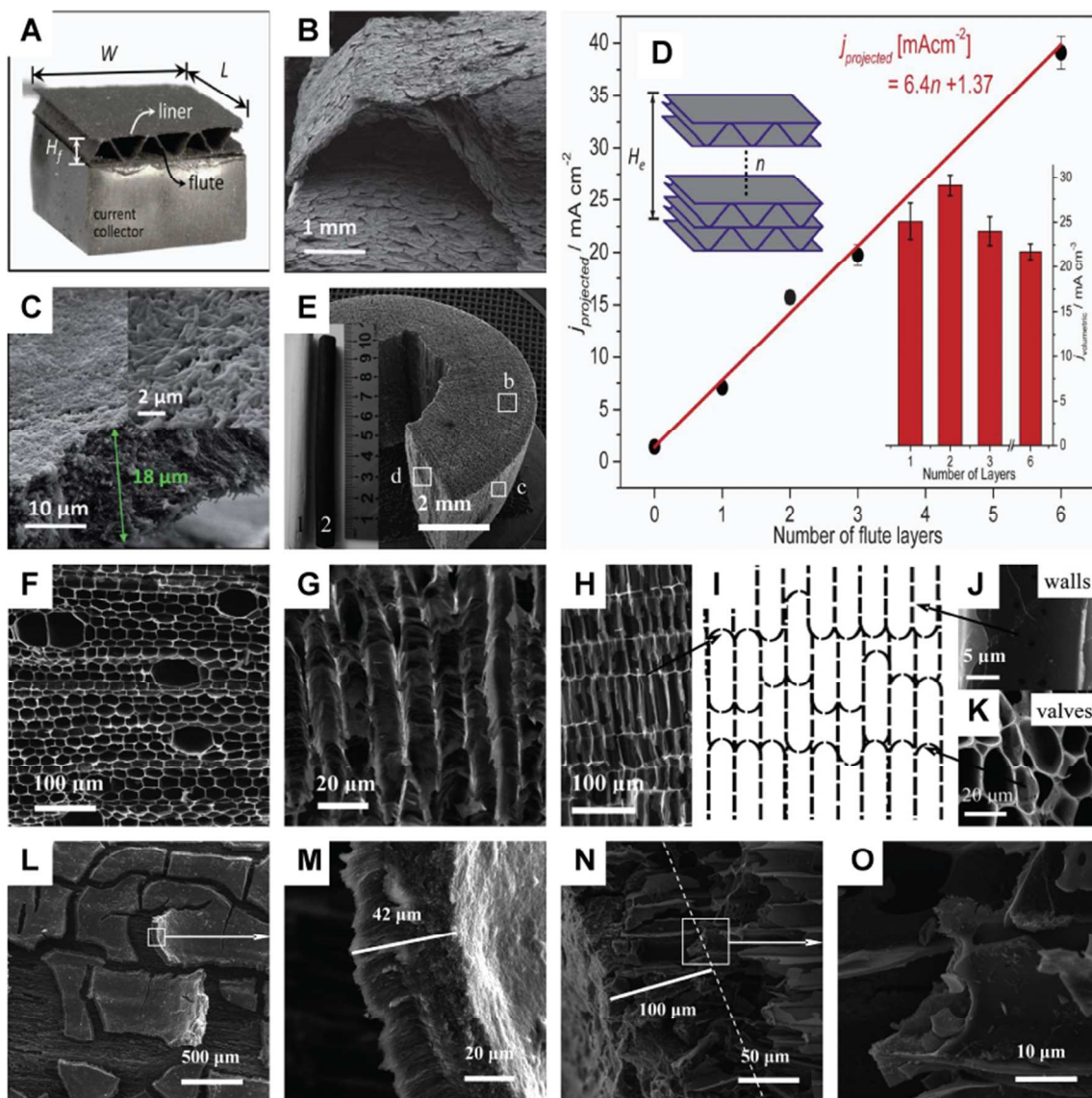


Figure 14. Non-sponge templated electrodes. (A) Photographic image of a single-layered corrugated carbon (LCC) electrode (H_f , 1.4 mm; W , 10 mm; L , 10 mm). (B, C) SEM images of the colonized LCC electrode. (D) Dependence of current densities on the number of flute layers.⁶⁴ (E) Physical image of a piece of cleaved 3D-KSC electrode. Insets show the kenaf stalk before (1) and after (2) carbonization. (F) Vertical sectioned SEM image at position (b). (G) SEM image at position (c). (H) Longitudinal sectioned SEM image at position (d). (I) Schematic of the inner structure of the 3D-KSC. (J, K) SEM images of the channel walls (J) and vales (K). (L–O) SEM images of the colonized 3D-KSC electrode.⁵⁶ Reproduced with permission from Wiley.

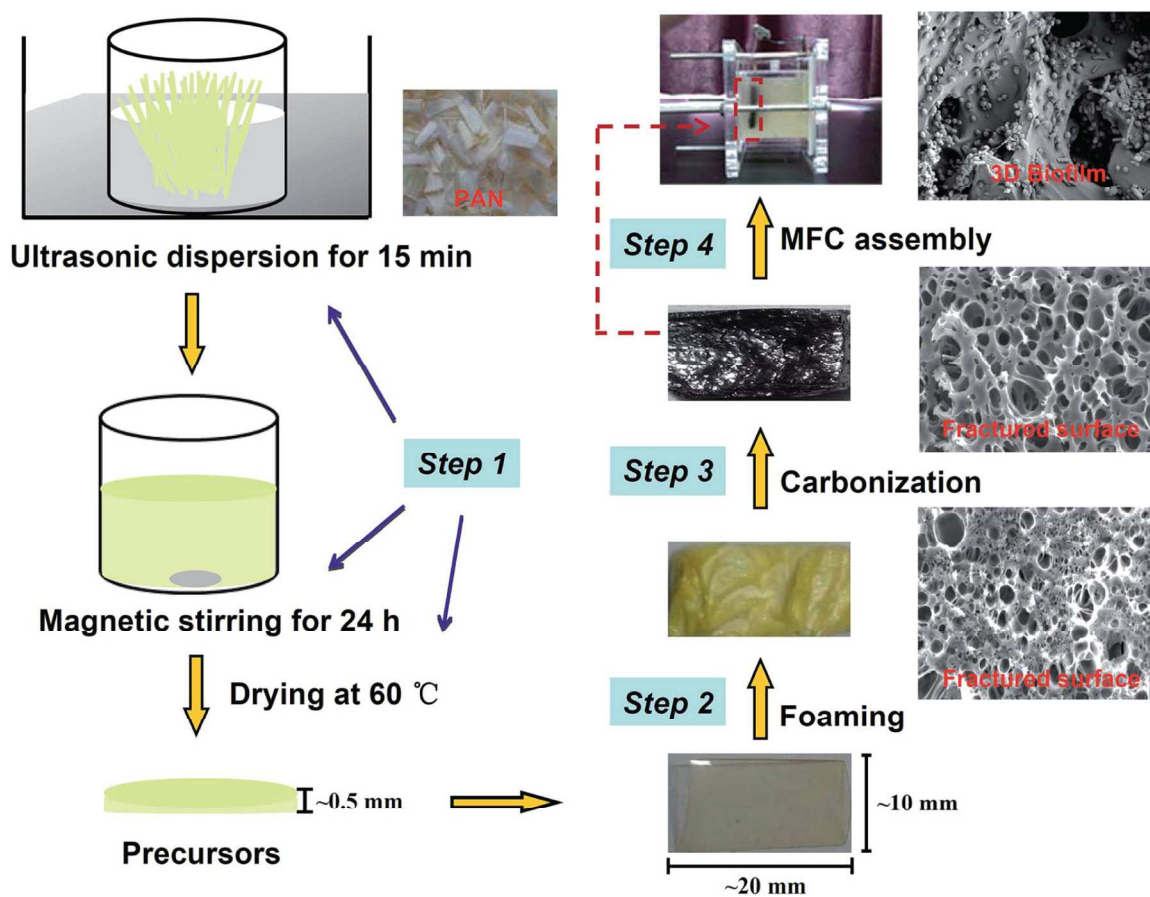


Figure 15. Schematics of 3D open-celled carbon scaffold anode preparation and MFC assembly.⁶¹

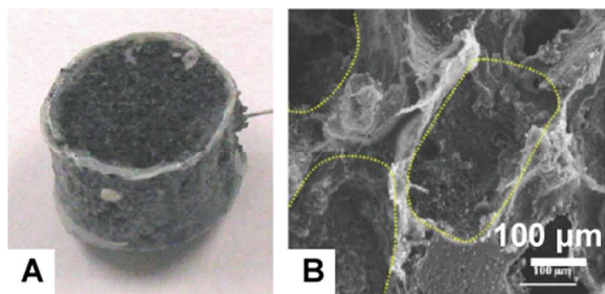


Figure 16. Polymer/carbon composite electrode prepared by a solvent cast and particulate leaching process. (A) Physical image. (B) SEM image. Dashed lines indicate the holes left by the dissolved sucrose particles.⁷³ Reproduced with permission from American Chemical Society.

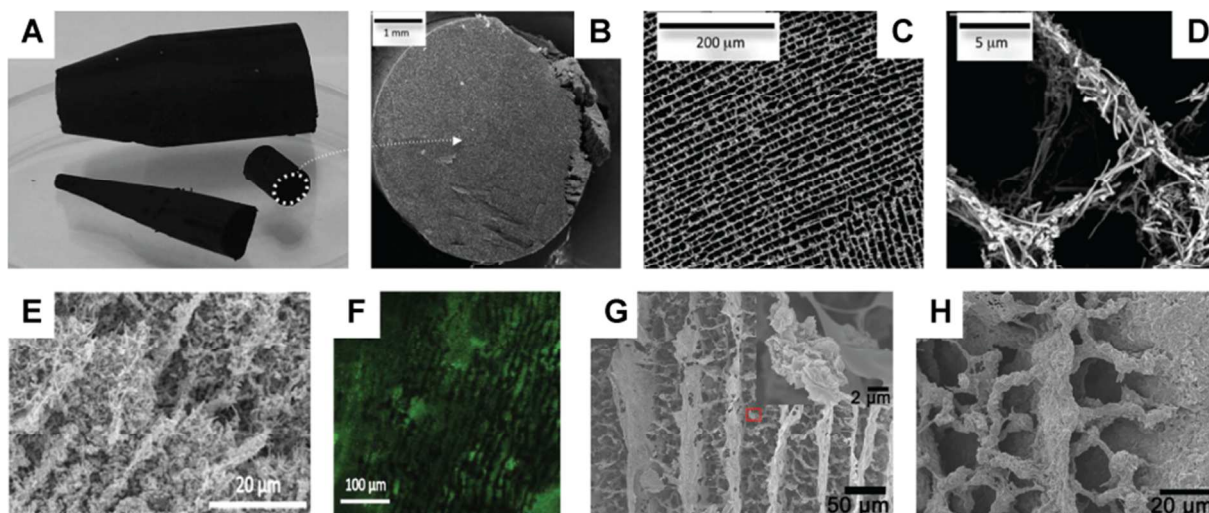
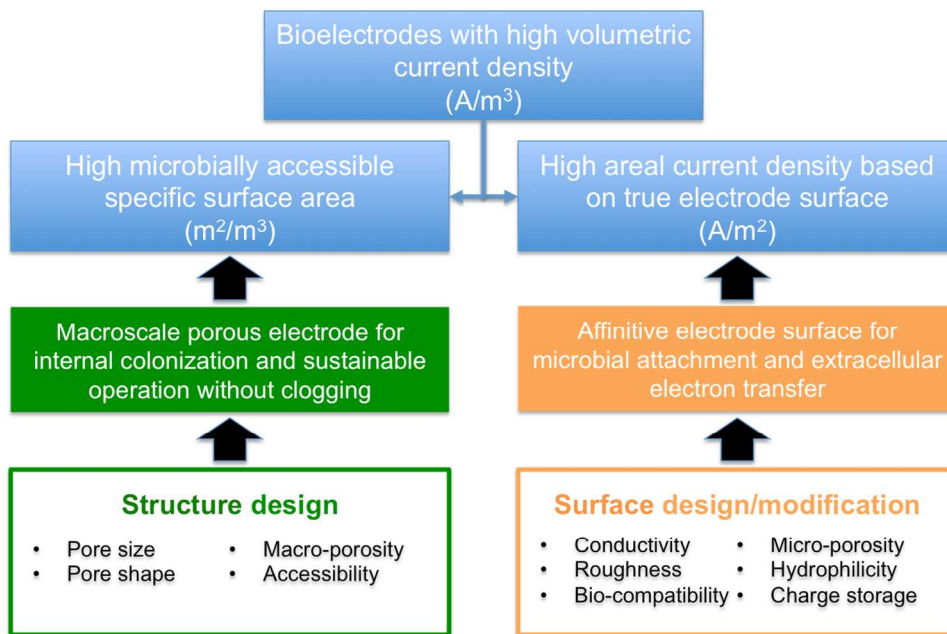
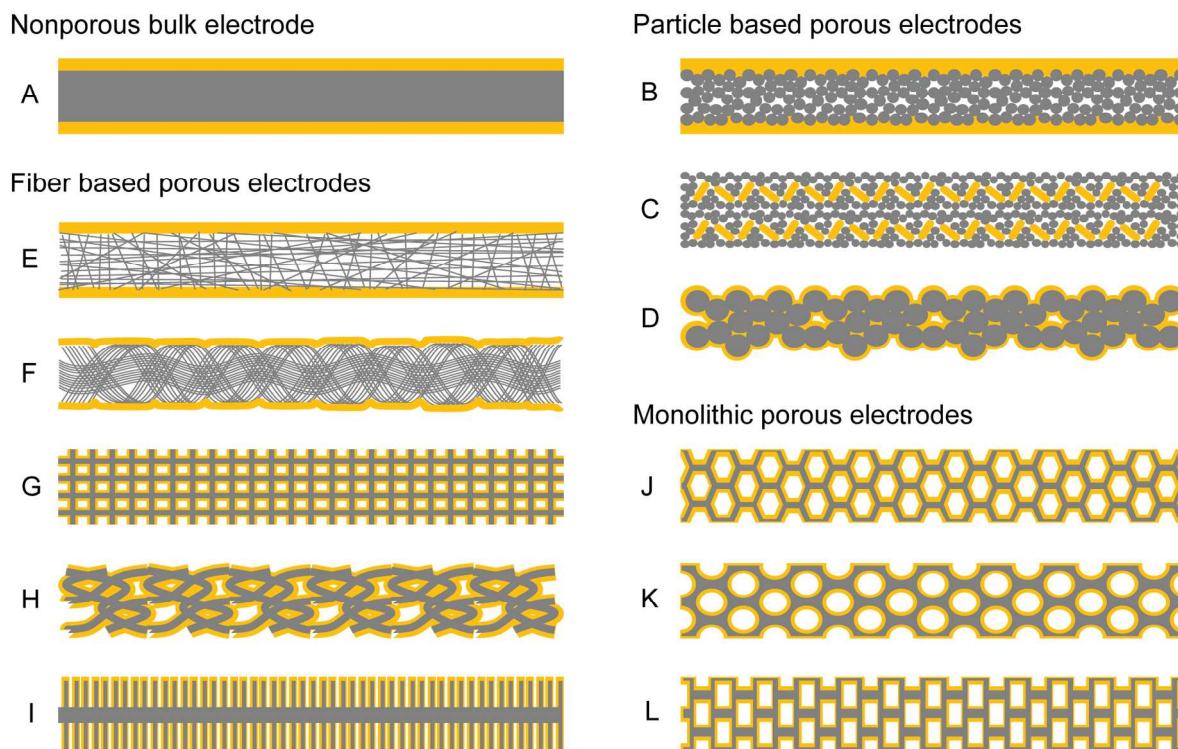


Figure 17. Composite electrodes prepared by ice segregation induced self-assembly (ISISA). (A-D) Physical image (A) and SEM images (B-D) of MWCNT/chitosan composite electrodes. (E) SEM image of colonized MWCNT/chitosan electrode. (F) Confocal laser scanning microscopy image of the colonized MWCNT/chitosan electrode.⁷⁵ (G, H) Vacuum-stripped graphene (VSG)/chitosan composite electrode before (G) and after (H) colonization.⁷⁶ Reproduced with permission from American Chemical Society.



Scheme 1. Goal and strategy of developing high-performance bioelectrodes.



Scheme 2. Configuration of bioelectrodes. The grey color indicates electrode materials and the orange color indicates microbial biofilms. (A) Nonporous bulk electrode. (B-D) Particle based porous electrodes, including densely piled electrode (B), cell-embedded electrode (C), and packed bed electrode (D). (E-I) Fiber based porous electrodes, including carbon paper electrode (E), carbon cloth or nanofiber sheet electrode (F), stainless steel mesh electrode (G), carbon felt or CNT-coated textile electrode (H), and carbon brush electrode (I). (J-L) Monolithic porous electrodes prepared by carbonization or conductive surface modification of porous templates (J), by solvent cast and particulate leaching (K), and by ice segregation induced self-assembly (L).

Table 1. Examples of microbially-mediated half reactions of significance for electron transfer from solids, ranked by energy per electron equivalent, from strongest electron donor to weakest (298 K, pH 7).

e^- donor	Half reactions ranked by electron donor strength	E° (V)
Organic matter	$\frac{1}{e}C_aH_bO_cN_d + \frac{2a-c}{e}H_2O = \frac{a}{e}CO_2 + \frac{d}{e}NH_3 + H^+ + e^-$	-0.42
	where $e=4a+b-2c-3d$	to -0.20
H ₂	$2H^+ + 2e^- = H_2$	-0.41
HS ⁻	$SO_4^{2-} + 9H^+ + 8e^- = HS^- + 4H_2O$	-0.22
S	$SO_4^{2-} + 8H^+ + 6e^- = S + 4H_2O$	-0.20
AsO ₃ ³⁻	$AsO_4^{3-} + 4H^+ + 2e^- = H_2AsO_3^- + H_2O$	+0.15
Se	$SeO_4^{2-} + 8H^+ + 6e^- = Se + 4H_2O$	+0.33
NH ₄ ⁺	$NO_3^- + 10H^+ + 8e^- = NH_4^+ + 3H_2O$	+0.36
Mn (II)	$MnO_2 + 4H^+ + 2e^- = Mn^{2+} + 2H_2O$	+0.47
U(IV)	$UO_2(CO_3)_3^{4-} + 3.52H^+ + 2e^- = UO_2 + 2.48HCO_3^- + 0.52H_2CO_3$	+0.59

Table 2. Examples of microbially-mediated half reactions of significance for electron transfer to solids, ranked by energy per electron equivalent, from strongest electron acceptor to weakest (298 K, pH 7).

e^- acceptor	Half reactions ranked by electron acceptor strength	E° (V)
N_2O	$N_2O + 2H^+ + 2e^- = N_2 + H_2O$	+1.35
BrO_3^-	$BrO_3^- + 6H^+ + 5e^- = 0.5Br_2 + 3H_2O$	+1.11
MnO_4^-	$MnO_4^- + 8H^+ + 5e^- = Mn^{2+} + 4H_2O$	+1.10
ClO_3^-	$ClO_3^- + 6H^+ + 5e^- = 0.5Cl_2 + 3H_2O$	+1.06
Fe(III)	$Fe(OH)_3 + 0.17H_2CO_3 + 0.83HCO_3^- + 1.83H^+ + e^- = FeCO_3 + 3H_2O$	+0.96
NO_2^-	$2NO_2^- + 8H^+ + 6e^- = N_2 + 4H_2O$	+0.94
$Cr_2O_7^{2-}$	$Cr_2O_7^{2-} + 14H^+ + 6e^- = 2Cr^{3+} + 7H_2O$	+0.92
Fe(III)	$Fe(OH)_3 + 3H^+ + e^- = Fe^{2+} + 3H_2O$	+0.85
O_2	$O_2 + 4H^+ + 4e^- = 2H_2O$	+0.82
ClO_4^-	$ClO_4^- + 2H^+ + 2e^- = ClO_3^- + H_2O$	+0.82
MnO_2	$MnO_2 + 4H^+ + 2e^- = Mn^{2+} + 2H_2O$	+0.81
NO_3^-	$2NO_3^- + 12H^+ + 10e^- = N_2 + 6H_2O$	+0.74
U(VI)	$0.5UO_2(CO_3)_3^{4-} + 1.76H^+ + e^- = 0.5UO_2 + 1.24HCO_3^- + 0.26H_2CO_3$	+0.59
NO_3^-	$NO_3^- + 2H^+ + 2e^- = NO_2^- + H_2O$	+0.43
NO_3^-	$NO_3^- + 10H^+ + 8e^- = NH_4^+ + 3H_2O$	+0.36
SeO_4^{2-}	$SeO_4^{2-} + 8H^+ + 6e^- = Se + 4H_2O$	+0.33
$C_6H_4ClCOO^-$	$C_6H_4ClCOO^- + H^+ + 2e^- = C_6H_5COO^- + Cl^-$	+0.26
$(CH_3)_2SO$	$(CH_3)_2SO + 2H^+ + 2e^- = (CH_3)_2S + H_2O$	+0.23
$S_2O_3^{2-}$	$S_2O_3^{2-} + 8H^+ + 8e^- = 2HS^- + 3H_2O$	-0.21
SO_4^{2-}	$SO_4^{2-} + 9H^+ + 8e^- = HS^- + 4H_2O$	-0.22
CO_2	$CO_2 + 8H^+ + 8e^- = CH_4 + 2H_2O$	-0.24
S	$S + H^+ + 2e^- = HS^-$	-0.27

Table 3. Spreading time for dissolved solutes as function of distance. Assumed coefficient of molecular diffusion $D = 10^{-9} \text{ m}^2/\text{s}$. Spreading in time t is $t = L^2/2D$, where L is the diffusion distance.

Diffusion Distance	Time Required
1 μm (scale of a bacterium)	$0.5 \times 10^{-3} \text{ s}$
1 mm	8 min
1 cm	0.6 day
10 cm	2 months

Table 4. Examples of bioelectrodes invested in BESs.

Bioelectrodes for BESs	Microorganism	Feed	Current density	Measurement	Refs
Nonporous bulk electrodes					
Graphite	Mixed	Acetate	10 A/m ²	at -0.35 V vs. Ag/AgCl	95
Glassy carbon + MWCNTs	<i>S. oneidensis</i>	LB broth	~0.1 A/m ²	at 0 V vs. Ag/AgCl	96
Glassy carbon + MWCNTs/SnO ₂	<i>E. coli</i>	Glucose	3.5 A/m ²	Polarization curve	97
Graphite + MWCNTs/MnO ₂	Mixed	Sediment	~0.45 A/m ²	Polarization curve	98
Graphite + graphene	Mixed	Acetate	~2.7 A/m ²	Polarization curve	99
Graphite + polyaniline/vanadate	Mixed	Sediment	~0.65 A/m ²	Polarization curve	103
Graphite + carbon/polymer	Mixed	Acetate	1 A/m ²	Polarization curve	104
Gold	<i>G. sulfurreducens</i>	Acetate	0.4-0.7 A/m ²	at 0.3 V vs. Ag/AgCl	9
Gold	<i>G. sulfurreducens</i>	Acetate	4 A/m ²	at 0.24 V vs. SHE	106
Gold line array	<i>G. sulfurreducens</i>	Acetate	16 A/m ²	at 0.24 V vs. SHE	106
Pt/Ti	Mixed	Acetate	4.1 A/m ²	Polarization curve	107
Stainless steel	Mixed	Acetate	4 A/m ²	at -0.1 V vs. SCE	72
Gold	Mixed	Acetate	11.75 A/m ²	at 0.2 V vs. Ag/AgCl	94
Silver	Mixed	Acetate	11.19 A/m ²	at 0.2 V vs. Ag/AgCl	94
Copper	Mixed	Acetate	15.15 A/m ²	at -0.2 V vs. Ag/AgCl	94
Stainless steel	Mixed	Acetate	6.74 A/m ²	at -0.2 V vs. Ag/AgCl	94
Nickel	Mixed	Acetate	3.84 A/m ²	at -0.2 V vs. Ag/AgCl	94
Particle based porous electrodes					
Graphite	<i>E. coli</i>	Glucose	1.2 A/m ²	over 1.98 kΩ	111
Graphene	<i>E. coli</i>	Glucose	5.8 A/m ²	Polarization curve	112
Activated carbon/goethite	Mixed	Acetate	3.6 A/m ²	Polarization curve	113
Polyaniline/WO ₃	<i>E. coli</i>	Glucose	~9 A/m ²	Polarization curve	10
Mo ₂ C/CNTs	<i>E. coli</i>	Glucose	~19 A/m ²	Polarization curve	114
MWCNTs/polyaniline	<i>E. coli</i>	Glucose	~0.15 A/m ²	Polarization curve	116
TiO ₂ /polyaniline	<i>E. coli</i>	Glucose	~8 A/m ²	Polarization curve	115
Graphene/TiO ₂	<i>S. oneidensis</i>	Lactate	~4.2 A/m ²	Polarization curve	117
Carbon nanoparticles/bacteria	Mixed	Acetate	~9 A/m ²	Polarization curve	118
Graphene/bacteria	Mixed	Acetate	~9 A/m ²	Polarization curve	121
<i>E. coli</i> /Fe ₃ O ₄ /CNTs	<i>E. coli</i>	Glucose	~2.2 A/m ²	Polarization curve	122
Graphite granules	Mixed	Acetate	80 A/m ³	over 20 Ω	69
Graphite granules	Mixed	Acetate	~150-250 A/m ³	over 10.5-50 Ω	70
Graphite coated crumb rubber granules	Mixed	Acetate	~1 A/m ³	Polarization curve	71
Fiber based porous electrodes					
Carbon paper + Pt/MWCNTs	<i>E. coli</i>	Glucose	~8 A/m ²	Polarization curve	126
Carbon paper + polypyrrole/MWCNTs	<i>E. coli</i>	Glucose	~1.7 A/m ²	Polarization curve	127
Carbon paper + graphene/Au	<i>S. oneidensis</i>	Lactate	1.8 A/m ²	at 0.2 V vs. Ag/AgCl	129
Carbon paper + plasma	Mixed	Acetate	~0.2 A/m ²	Polarization curve	129
Carbon paper + mesoporous carbon	Mixed	Glucose	~0.8 A/m ²	over 500 Ω	130
Carbon paper + CNTs	<i>S. oneidensis</i>	Lactate	2.65 A/m ²	at 0.1 V vs. Ag/AgCl	132
Carbon paper + graphene	Mixed	Glucose	~0.4 A/m ²	over 1 kΩ	131
Carbon cloth + polyaniline/graphene	Mixed	Acetate	3.4 A/m ²	Polarization curve	135
Carbon cloth + polyaniline	Mixed	Acetate	~0.3 A/m ²	over 510 Ω	136
Carbon cloth + polypyrrole	Mixed	Acetate	3.5 A/m ²	Polarization curve	137
Carbon cloth + MWCNTs	Mixed	Acetate	~0.73 A/m ²	Polarization curve	138
Carbon cloth + N-doped CNTs	Mixed	Acetate	3.63 A/m ²	over 10 Ω	139
Carbon cloth + graphene	<i>P. aeruginosa</i>	Glucose	0.245 A/m ²	over 1.96 kΩ	140
Carbon cloth + graphene/SnO ₂	<i>E. coli</i>	Glucose	~3.4 A/m ²	Polarization curve	142
Carbon cloth + anodisation	Mixed	Acetate	~3 A/m ²	Polarization curve	145
Carbon cloth + anodisation	Mixed	Acetate	6.7 A/m ²	over 30 Ω	146
Carbon mesh	Mixed	Acetate	~5 A/m ²	Polarization curve	148
Stainless steel mesh	Mixed	Acetate	8.2 A/m ²	at -0.1 V vs. SCE	72
Stainless steel mesh + MWCNTs	Mixed	Acetate	~6 A/m ²	Polarization curve	90
Carbon felt + carbon/polymers	Mixed	Wastewater	0.11 A/m ²	over 10 kΩ	152
Carbon felt + porous carbon	<i>E. coli</i>	Glucose	13.4 A/m ²	Polarization curve	153
Carbon felt + CNTs	Mixed	Mixture [#]	5 A/m ² , ~1.7 kA/m ³	Polarization curve	79
Carbon felt + CNTs	Mixed	Acetate	35.7 A/m ²	at 0.2 V vs. Ag/AgCl	78
Carbon felt + anodisation	Mixed	Dairy waste	1.6 A/m ²	at 0.1 V vs. SCE	88
Carbon felt + mediator	<i>G. sulfurreducens</i>	Acetate	12 A/m ² , 6 kA/m ³	at 0.04 V vs. NHE	87
Carbon felt + polymer	Mixed	Acetate	10 A/m ² , 5 kA/m ³	over 1 kΩ	86
Carbon felt + RuO ₂	<i>S. oneidensis</i>	Lactate	13 A/m ² , 2.6 kA/m ³	Polarization curve	85
Carbon felt + MnO ₂	Mixed	Acetate	18.73 A/m ² , 3.75 kA/m ³	Polarization curve	84
Carbon felt + polypyrrole/CNTs	Mixed	Acetate	1.6 A/m ² , 530 A/m ³	over 200 Ω	83
Carbon felt + polyaniline/CNTs	<i>S. putrefaciens</i>	Acetate	~1.7 A/m ² , ~860 A/m ³	over 1.96 kΩ	82
Carbon felt + polypyrrole/graphene	<i>S. oneidensis</i>	Lactate	~18 A/m ² , ~3.6 kA/m ³	Polarization curve	81
Carbon felt + polyaniline	Mixed	Mixture [#]	25 A/m ²	Polarization curve	80
Carbon brush	Mixed	Acetate	~1 kA/m ³	Polarization curve	74
CNT-textile	Mixed	Glucose	14.4 A/m ² , 7.2 kA/m ³	Polarization curve	23
Carbonized textile	Mixed	Acetate	8 A/m ²	at 0.3 V vs. Ag/AgCl	65
Carbon fiber network	Mixed	Acetate	30 A/m ²	at 0.2 V vs. Ag/AgCl	31
Activated carbon fiber network	Mixed	Wastewater	2.7 kA/m ³	Polarization curve	63
Monolithic porous electrodes					
RVC	Mixed	Sucrose	50 A/m ³	Polarization curve	66
RVC	<i>S. oneidensis</i>	Lactate	0.1 A/m ² ###, 600 A/m ³	Short circuit current	67
RVC + CNTs	Mixed	Acetate	0.4 A/m ² ###, 10.3 kA/m ³	at 0 V vs. Ag/AgCl	89

CNT-sponge	Mixed	Glucose	21.3 A/m ² , 10.6 kA/m ³	Polarization curve	50
Graphene/polyaniline foam	<i>S. oneidensis</i>	Lactate	5 A/m ² , 5 kA/m ³	Polarization curve	8
Carbonized corrugated fiberboard	Mixed	Acetate	390 A/m ² , 32 kA/m ³	at 0.2 V vs. Ag/AgCl	64
Carbonized kenaf stem	Mixed	Acetate	32.5 A/m ²	at 0.2 V vs. Ag/AgCl	56
Carbonized pomelo peel	Mixed	Acetate	>40 A/m ² , 18.7 kA/m ³	at 0.2 V vs. Ag/AgCl	57
Carbonized corn stem	Mixed	Acetate	31.2 A/m ² , 15.6 kA/m ³	at 0.2 V vs. Ag/AgCl	58
Carbonized king mushroom	Mixed	Acetate	20.9 A/m ² , 10.5 kA/m ³	at 0.2 V vs. Ag/AgCl	58
Carbonized wild mushroom	Mixed	Acetate	30.2 A/m ² , 15.1 kA/m ³	at 0.2 V vs. Ag/AgCl	58
Carbonized tubular bamboo	Mixed	Acetate	~5 A/m ²	Polarization curve	59
Carbonized loofah sponge	Mixed	Acetate	1.9 A/m ² , 380 A/m ³	over 1 kΩ	60
CNT-polysulfone matrix	<i>S. oneidensis</i>	Lactate	1.5 A/m ²	over 2 kΩ	68
Carbonized polyacrylonitrile/graphite	<i>E. coli</i>	Glucose	2.91 A/m ² , 2.91 kA/m ³	Polarization curve	61
Graphite/PHBV by SCPL	<i>S. oneidensis</i>	Lactate	22.18±6.69 A/m ³	Polarization curve	73
MWCNT/Chitosan by ISISA	<i>G. sulfurreducens</i>	Acetate	24.5 A/m ² , 19 kA/m ³	at 0 V vs. Ag/AgCl	75
VSG/Chitosan by ISISA	<i>P. aeruginosa</i>	Glucose	2.55 A/m ²	over 1.96 kΩ	76
Graphene by ISISA	Mixed	Acetate	3 kA/m ³	Polarization curve	77
Ti ₄ O ₇ by ISISA	<i>G. sulfurreducens</i>	Acetate	128.7 A/m ² , 9.5 kA/m ³	at 0.2 V vs. Ag/AgCl	62

Starch, peptone, and fish extract; ## Based on true surface area.

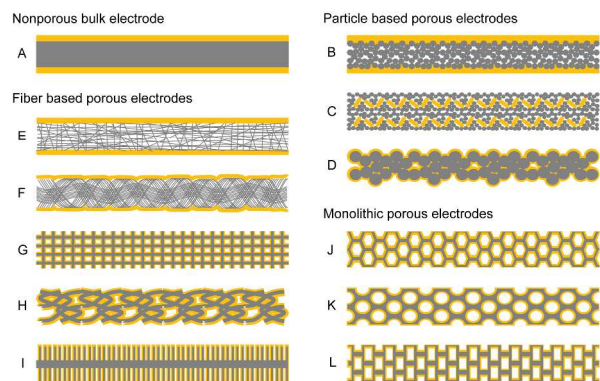
MWCNT, multi-walled carbon nanotube; RVC, reticulated vitreous carbon; PHBV, poly 3-hydroxybutyrate-co-3-hydroxyvalerate;

SCPL, solvent cast and particulate leaching; ISISA, ice segregation induced self-assembly; VSG, vacuum-stripped graphene.

Broader context

Microbial bioelectrochemical systems (BESs) interconvert electrical and chemical energy. The key component of a BES is a bioelectrode colonized by microorganisms that function as living “catalysts” for electron transfer. The activity of these organisms is critical and controlled by efficient delivery of reactants, efficient transfer of electrons to or from cells to the bioelectrode, and removal of products. For optimal microbial activity, the bioelectrode requires a porous structure with large accessible surface area and an affinitive electrode surface for efficient extracellular electron transfer. Scientists have developed bioelectrodes that achieve high current outputs, but long-term studies are critical, and capital cost is a concern for large-scale BES applications. At present, most existing high-performance bioelectrodes use expensive materials or require complex and energy-consuming synthetic steps. Development of stable and cost-effective porous electrodes remains a high priority.

Table of contents entry



Schematic of microbial bioelectrodes with different configurations.